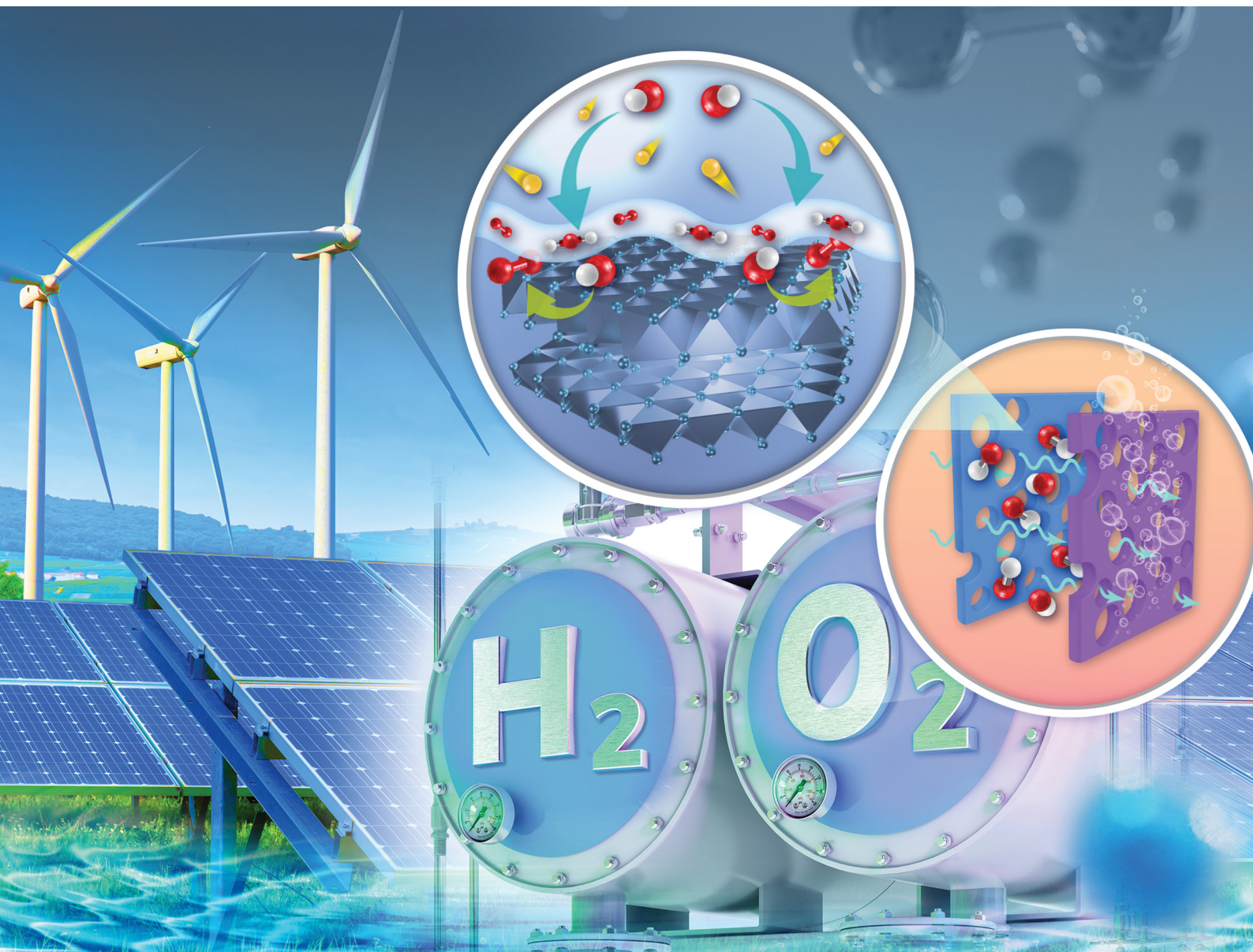


EES Catalysis

rsc.li/EESCatalysis



ISSN 2753-801X














PAPER

Deborah J. Myers, Raphaël P. Hermann *et al.*
Synergy between Ni and Fe in NiFe aerogel oxygen
evolution reaction catalyst: *in situ* ^{57}Fe Mössbauer
and X-ray absorption spectroscopy studies



Cite this: *EES Catal.*, 2025,
3, 1229

Synergy between Ni and Fe in NiFe aerogel oxygen evolution reaction catalyst: *in situ* ⁵⁷Fe Mössbauer and X-ray absorption spectroscopy studies†‡

Haoran Yu, ^a Matthew E. Sweers, ^b Luigi Osmieri, ^c Jae Hyung Park, ^b A. Jeremy Kropf, ^b Dali Yang, ^d Lu Ma, ^d Xiang Lyu, ^e Alexey Serov, ^e David A. Cullen, ^a Piotr Zelenay, ^c Deborah J. Myers ^{*b} and Raphaël P. Hermann ^{*f}

Anion-exchange-membrane water electrolyzers (AEMWE) for hydrogen production have attracted interest because cost-effective Ni- and Fe-based catalysts can be used for the oxygen evolution reaction (OER). Although NiFe oxide/hydroxide-based catalysts have been extensively studied, the role of Fe and its chemical state during OER are not well understood, with inconsistent findings across different studies. In this work, we combined *in situ* ⁵⁷Fe Mössbauer (MS) and X-ray absorption spectroscopy (XAS) to investigate the chemical states of Fe and Ni and elucidate their synergy during the OER. A NiFe (8:1 molar ratio) aerogel catalyst with high surface area, nano crystallinity, and high performance in AEMWE was used. We show that both Fe and Ni are oxidized during anodic polarization, and the potential for the change of oxidation states correlates well with the onset of the OER. *In situ* MS shows that 80–90% of Fe³⁺ becomes tetravalent at OER potentials and remains so even after the potential is lowered below OER onset. Analysis of *in situ* XAS results suggests full Fe incorporation into Ni hydroxide. At OER potentials, lattice contraction indicates high oxidation states for both Ni and Fe. Upon returning to lower potentials, a portion of the Fe remains in its more oxidized form which corroborates the *in situ* MS findings. Results from this work affirm the importance of high-valent Ni and Fe in promoting the OER. Ni and Fe exhibit synergy during OER and the aerogel's unique nanomorphology leads to high OER activity.

Received 25th April 2025,
Accepted 15th May 2025

DOI: 10.1039/d5ey00127g

rsc.li/eescatalysis

Broader context

Water electrolysis (WE) is an efficient technology to store excess electricity in hydrogen for use in various applications and industries. The high cost of platinum-group-metal catalysts for oxygen evolution reaction (OER) is a bottleneck for current WE technology. Ni- and Fe-hydroxide based OER catalysts promise significant cost reduction for new anion exchange membrane (AEM) WE technology. There is a pressing need to understand the structure-performance relationships for these catalysts, in particular the role and oxidation state of Fe during OER. Here, we combine *in situ* ⁵⁷Fe Mössbauer (MS) and X-ray absorption spectroscopy (XAS) to show that the onset of OER correlates with the oxidation of Fe and Ni in a high-surface-area Ni/Fe hydroxide aerogel catalyst. The conversion of trivalent to tetravalent Fe reaches 90%, double that previously reported. This is ascribed to the unique nanosheet structure of the aerogel, providing high accessibility of Fe and Ni sites. In agreement with previous modeling studies, we provide strong evidence for tetravalent-Fe-mediated synergy of Fe and Ni redox processes during OER water electrolysis.

^a Center for Nanophase Materials Sciences, Oak Ridge National Laboratory, Oak Ridge, TN 37831, USA

^b Chemical Sciences and Engineering Division, Argonne National Laboratory, Lemont, IL 60439, USA. E-mail: dmyers@anl.gov

^c MPA-11, Materials Physics and Applications Division, Los Alamos National Laboratory, Los Alamos, NM 87545, USA

^d National Synchrotron Light Source II, Brookhaven National Laboratory, Upton, NY 39601, USA

^e Electrification and Energy Infrastructures Division, Oak Ridge National Laboratory, Oak Ridge, TN 37831, USA

^f Materials Science and Technology Division, Oak Ridge National Laboratory, Oak Ridge, TN 37831, USA. E-mail: hermannrp@ornl.gov

† This manuscript has been authored by UT-Battelle, LLC, under contract DE-AC05-00OR22725 with the US Department of Energy (DOE). The US government retains and the publisher, by accepting the article for publication, acknowledges that the US government retains a nonexclusive, paid-up, irrevocable, worldwide license to publish or reproduce the published form of this manuscript, or allow others to do so, for US government purposes. DOE will provide public access to these results of federally sponsored research in accordance with the DOE Public Access Plan (<https://energy.gov/downloads/doe-public-access-plan>).

‡ Electronic supplementary information (ESI) available. See DOI: <https://doi.org/10.1039/d5ey00127g>

§ These authors contributed equally.



Introduction

Water electrolyzers are being deployed to store excess electricity in the chemical bonds of hydrogen. Hydrogen can then be used in a variety of applications, such as petroleum refining, ammonia production, and as a fuel for stationary and mobile power generation. At present, liquid alkaline (LA) and proton exchange membrane (PEM) water electrolyzers (WE) are the most industrialized electrolysis technologies.^{1,2} PEMWEs operate at higher current and have higher efficiency than LAWE, but require expensive noble-metal catalysts for both the oxygen evolution and hydrogen evolution reactions.³ Whereas cost reduction for PEMWEs is expected from a variety of strategies – including scale up, operation optimization, and advanced manufacturing – reducing the use of noble-metal catalysts is crucial due to their scarcity and vulnerable supply chains.⁴ Therefore, there is increased interest in alternative technologies that combine the benefits of PEMWE and LAWE and broaden the choice of catalyst materials, such as anion exchange membrane water electrolyzers (AEMWEs). The alkaline environment of AEMWEs allows the use of non-noble-metal catalysts for the oxygen evolution reaction (OER), such as those comprised of Ni, Co, and Fe, which significantly reduces their capital cost compared to PEMWEs.^{5–9}

A schematic diagram of an AEM water electrolyzer is shown in Fig. 1. Alkaline electrolyte, typically dilute aqueous solution of potassium hydroxide (KOH), 0.1 to 1.0 M in concentration, is fed to the anode where OH[−] hydroxyl ions are oxidized, generating oxygen and water. Water diffuses through the AEM from the anode to the cathode, where it is reduced to hydrogen and

hydroxyl ions. Hydroxyl ions then diffuse back to the anode through the AEM allowing an internal flow of ions, balancing the external flow of electrons from the power supply.⁶ In AEM systems, the reaction kinetics on both the anode and cathode are slower than in PEM systems leading to a plethora of research devoted to the development of new catalysts and the understanding of reaction mechanisms.^{5,8}

The OER activity and mechanisms of Ni- and Fe-based catalysts have been extensively studied, as briefly summarized here. Comprehensive reviews on the topic can be found in Dionigi *et al.*¹⁰ and Anantharaj *et al.*¹¹ An early study from Mlynarek *et al.*¹² revealed that adding Fe into Ni hydroxide *via* surface contamination or co-precipitation significantly reduced the overpotential for the OER. This effect was attributed to the enhancement of electronic conductivity.¹² Such enhancement of OER activity was further studied using *in situ* Mössbauer spectroscopy (MS) which suggested partial transfer of electronic density away from Fe(III) sites upon the oxidation of the Ni(II) sites, implying incorporation of Fe into the Ni hydroxide lattice resulting in enhanced OER activity *versus* the constituent hydroxides alone.¹³

Trotochaud *et al.*¹⁴ examined the effect of Fe doping and also concluded that Ni_{1−x}Fe_xOOH-based catalysts show OER activity superior to that of Ni oxyhydroxide. Similarly, the addition of Fe to Co (oxy)hydroxide has been found to improve its OER activity.^{15,16} The underlying mechanism and the role of Fe has been found to be more than that of simply enhancing electronic conductivity.^{17–22} For example, density functional theory (DFT) suggests that Fe reduces the binding energy of oxygen-containing intermediate species during the OER and

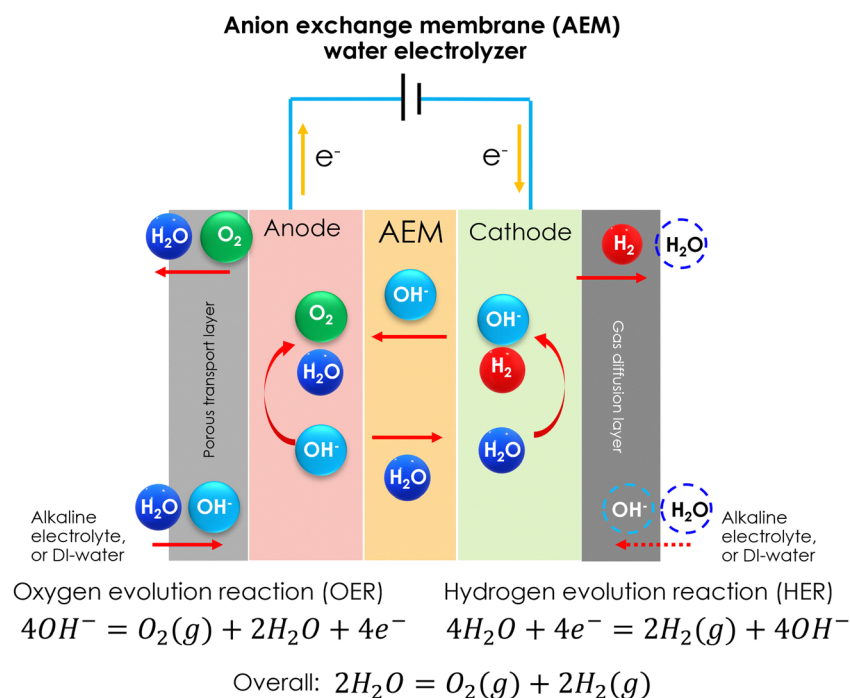


Fig. 1 Schematic of an anion exchange membrane (AEM) water electrolyzer. The system operates either by feeding KOH or de-ionized water to the anode, or to both the anode and cathode.



promotes the release of oxygen molecules. It was found that pure Ni sites are ineffective at producing O radicals, while high-spin $3d^4$ Fe(IV) stabilizes O radicals and generates them efficiently.²¹

The key elementary step of the OER is O–O coupling. There are three distinctive mechanisms describing the O–O coupling step: the adsorbate evolution mechanism (AEM), lattice oxygen mechanism (LOM) and intramolecular oxygen coupling (IMOC).^{23,24} AEM starts with the electrochemical oxidation of OH^- to $^*\text{OH}$, which is then deprotonated to $^*\text{O}$. The active $^*\text{O}$ exerts a nucleophilic attack on water molecules and forms $^*\text{OOH}$, completing the O–O coupling step. In the LOM, the bridging lattice oxygen delivers the O–O coupling together with the adsorbed $^*\text{OH}$ group, whereas IMOC delivers the O–O coupling through either neighboring adsorbed $^*\text{OH}$ groups or a $^*\text{OH}$ group and a $^*\text{O}$ radical.²⁴ Alternatively, IMOC is termed as an interaction of two M–O entity mechanisms (I2M)²⁵ or an oxide path mechanism (OPM).²⁶ Both, in fact, are referring to the same mechanism where direct O–O radical coupling occurs involving only $^*\text{O}$ and $^*\text{OH}$ intermediate species. Experimental work by the Strasser group confirmed the presence of the LOM path for NiFe layered double hydroxides.^{27,28} Recent theoretical work from the Goddard group²⁴ examined all three paths for O–O coupling and concluded that doping Fe into NiOOH shifts the reaction path from LOM toward AEM as the overpotential increases, which improves the stability of the catalyst as the consumption of lattice oxygen is decreased.²⁴

While oxidation of Fe(III) to Fe(IV) has been observed at OER potentials, the reported chemical state and role of Fe are not consistent across different studies. One group of studies reported that Fe remains as Fe(III) during the OER.^{20,29–35} Friebel *et al.*²⁹ and Görlin *et al.*^{32,33} reported only Fe(III) during the OER using *in situ* X-ray absorption spectroscopy (XAS). Friebel *et al.* concluded that Fe(III) centers serve as the OER active site by providing lower adsorption energies for OER intermediate species.²⁹ Klaus *et al.*³⁰ and Bates *et al.*³¹ also proposed that Fe is the sole active site for the OER. In contrast, Görlin *et al.*^{32,33} proposed that both Ni and Fe sites are active centers during the OER, but only observed Fe(III) in quasi-*in situ* XAS results (up to 1.63 V_{RHE}). Li *et al.*³⁴ proposed that incorporation of Fe(III) as a Lewis acid in Ni oxyhydroxide increases the acidity of OH_x moieties coordinated to Ni, resulting in more Ni(IV) and greater oxyl character of Ni(IV), thereby promoting O–O bond formation. Li *et al.*'s conclusions favor the Ni-only active site hypothesis.

Another group of studies^{16,21,36–40} observed the oxidation of Fe(III) to Fe(IV) during the OER. An early study by Balasubramanian *et al.*³⁶ using a co-deposited Fe and Ni thin film showed that incorporated Fe is further oxidized during the OER but remains in the lattice of γ -NiOOH. Chen *et al.*³⁷ and Kuang *et al.*³⁸ detected Fe(IV) species during the OER using *in situ* ^{57}Fe Mössbauer spectroscopy, reporting maxima of $\sim 20\%$ and $\sim 40\%$, respectively, of Fe in the Fe(IV) state. The oxidation of Fe was found to be concurrent with OER onset and Fe(IV) was reduced back to Fe(III) after removing the applied potential. Based on their *in situ* XAS experiments, Wang *et al.*⁴⁰ proposed

that the formation of a highly covalent Fe(IV)–O bond in the γ -NiOOH lattice facilitates charge transfer from Fe to Ni, resulting in higher valent Ni than that in pure Ni (oxy)hydroxide. Using DFT calculations, Goldsmith *et al.*³⁹ also concluded that charge is transferred from Fe to Ni. Fe(IV) is also observed in Co–Fe (oxy)hydroxide.¹⁶ Overall, high-valent metal oxide species were proposed to be beneficial for the nucleophilic attack of water, favoring the OER.

To help resolve these discrepancies about the behavior and role of iron and to broaden the understanding of Ni/Fe (oxy)hydroxides beyond thin film studies, we aim to investigate and understand the chemical state and structure of Ni and Fe in a high-surface-area Ni/Fe (oxy)hydroxide catalyst during OER. We combine *in situ* Mössbauer and XAS spectroscopies, techniques probing both the surface and bulk properties of materials, to elucidate the chemical state of Ni and Fe. Instead of commonly used electrodeposited NiFe (oxy)hydroxide thin films that are less suitable as electrodes for AEMWEs, we focus on a NiFe-based aerogel catalyst which has demonstrated excellent performance and durability in AEMWEs.^{41,42} The aerogel catalyst was stable in an AEM electrolyzer test for at least 110 hours at 1 A cm^{-2} in 1 M KOH at 80 °C.⁴¹ Here, *in situ* ^{57}Fe MS results obtained with a NiFe-based aerogel catalyst show formation of Fe species with higher oxidation state than Fe(III) at 1.45 V_{RHE} , concurrent with the onset of OER. The percentage of Fe(III) converted to tetravalent Fe ($\sim 90\%$) far exceeds percentages reported in the literature thus far,^{37,38} possibly due to the accessibility of Fe in this high-surface-area and highly porous aerogel. Furthermore, the tetravalent Fe was retained at open circuit potential (OCP) for ~ 24 hours after the experiment was concluded. *In situ* XAS studies were conducted in parallel to investigate the evolution of the Ni hydroxide structure and metal–oxygen bonding during the OER. At OER potentials, we observed transformation of the catalyst from an Fe-doped α -Ni(OH)₂ to an Fe-doped γ -NiOOH structure and an associated contraction of both Fe and Ni–O bonds indicative of the formation of high-valent Fe and Ni ($>90\%$ of Fe and Ni). Simultaneous oxidation of Ni and Fe occurs at the onset potential of OER, and both remain in high oxidation states throughout OER, and a fraction of Fe remains in the highly oxidized form when returning to potentials lower than the OER onset potential. The *in situ* MS and XAS findings support the model of synergy between Ni and Fe and that both Ni and Fe in high oxidation states are needed to promote OER in a high-surface-area Fe-doped Ni oxyhydroxide catalyst.

Experimental

Synthesis of the ^{57}Fe -enriched Ni₈Fe aerogel

The synthesis of the Ni–Fe aerogel catalysts is described in detail in our previous work.⁴¹ We slightly modified the previously described method to synthesize the ^{57}Fe -enriched catalysts needed for the *in situ* Mössbauer experiments because the ^{57}Fe precursor was Fe metal powder rather than the Fe(II) chloride used to synthesize the non-enriched catalyst. The ^{57}Fe



metal powder was purchased from Sigma Aldrich. To obtain FeCl₂, the ⁵⁷Fe metal powder (16.5 mg) was mixed with a stoichiometric amount of concentrated HCl solution (37 wt%, 0.05 mL) and the mixture was allowed to react for over 12 h. Once the reaction reached completion, *i.e.*, when all metallic Fe particles were consumed and H₂ bubbles were no longer observed, the solution was transferred to a glass vial where 550 mg of NiCl₂·6H₂O (Fisher Scientific) and 10 mg of polyacrylic acid (MW 450 000, Sigma Aldrich) were previously dissolved in 5.83 mL of ethanol (200 proof, Sigma Aldrich). The resulting Ni to Fe molar ratio in the solution was 8 to 1; the resulting catalyst is referred to as Ni₈Fe based on this nominal Ni to Fe ratio. Then 0.667 mL of propylene oxide (Sigma Aldrich) was slowly added, whereupon the vial was sealed and left to age for 48 hours to ensure gel formation. The gel was then washed several times with ethanol, followed by drying in an automated supercritical CO₂ dryer (Autosamdri-931, Tousimis, USA), as described in our previous work.⁴¹ The thus synthesized aerogel was used in the Mössbauer and XAS experiments without any additional treatment.

Electrode fabrication

An electrode ink was prepared using the Ni₈Fe catalyst, a 1 : 1 volume-ratio of deionized (DI) water and isopropanol (IPA) as a solvent, and a Nafion[®] suspension (D520, Ion Power Inc.) at an ionomer-to-catalyst ratio of 0.8. The mixture was sonicated in a bath sonicator for 1 hour. Prior to preparing the electrode ink, the Nafion[®] suspension was neutralized with 1 M NaOH and allowed to equilibrate overnight. A relatively high ionomer-to-catalyst ratio was employed compared to that used for conventional RDE testing (*e.g.*, 0.2) to enhance electrode adhesion. For both the *in situ* MS and X-ray absorption near-edge spectroscopy (XANES) experiments, the prepared electrode ink was deposited onto both sides of carbon paper (AvCarb 280) utilizing a custom-built auto-deposition system.⁴³ For the *in situ* extended X-ray absorption fine structure (EXAFS) experiments, the catalyst ink was deposited onto Kapton-encased graphene sheets (Ultra-Conductive Graphene Sheet, 25 μm thick, McMaster-Carr) to form 5 mm by 3 mm deposits, using the same deposition system. The catalyst loading was 0.8 mg cm⁻² for the MS and EXAFS measurements and 0.3 and 2.8 mg cm⁻² for the XANES measurements at the Ni and Fe K-edges, respectively. The carbon paper substrate is stable throughout the *in situ* experiments, see Note S1 (ESI[†]).

In situ ⁵⁷Fe Mössbauer spectroscopy

In situ MS experiments utilized a modified three-electrode Teflon cell (Fig. S1, ESI[†]) based on the PTFE cell for alkaline electrolyte from Pine Research Instrumentation, Inc. with a redesigned cell body. The cell featured 25 mm diameter apertures enabling the transmission of 14.4 keV gamma radiation. Kapton tape was used as outer windows, with a Teflon sheet as the inner window facing the electrolyte. The electrolyte path-length was 4.5 mm and the 14.4 keV gamma ray transmission for the filled cell was ~50% (Fig. S1, ESI[†]). A mercury/mercury oxide reference electrode (+0.92 V *vs.* RHE) was used and

calibrated against a HydroFlex[®] hydrogen reference electrode (Gaskatel Inc.). All potentials in this manuscript are referenced to the reversible hydrogen electrode (RHE). The room-temperature 0.1 M KOH electrolyte was circulated using a peristaltic pump (Gilson Inc.) at a flow rate of ~50 mL min⁻¹. The Ni₈Fe catalyst-coated carbon paper working electrode was placed in between two pieces of Pt/C-coated (TEC10E50E from TKK, 0.2 mg cm⁻² Pt loading) gas diffusion layers (Sigracet 29BC) which served as counter electrodes.

The electrochemical measurement started with five voltammetric cycles from 1.2 V to 1.55 V at 50 mV s⁻¹ to ensure the absence of electrical shorting. We intended to minimize the influence of the catalyst activation prior to the *in situ* test so that we could observe how the catalyst evolves from its pristine state to activated state during OER. Activation of the catalyst likely induces structural changes as will be shown in the present work. Analyzing the catalyst only after activation would therefore overlook the structural changes that this work is targeting to reveal. The working electrode potential was then stepped from 1.25 V to 1.35 V, followed by 50 mV potential steps up to 1.75 V. The potential was then decreased to 1.4 V in 50 mV steps. Each potential was held for 3.5 hours while acquiring Mössbauer data to ensure good signal to noise ratios in the Mössbauer spectra. After the potential-controlled experiments were completed, Mössbauer spectra were acquired for approximately 24 hours at open circuit until the spectrum returned to a shape resembling what was recorded at the beginning of the test (at 1.25 V).

Mössbauer spectra were collected in the ±4 mm s⁻¹ velocity range, using a 10 mCi ⁵⁷Co@Rh source (Rietverc) and a Krypton gas proportional counter as the detector, with both the 14.4 keV and its signature Kr-escape peak selected as input for the multichannel analyzer. Approximately 240 000 counts are registered in 3.5 hours on a 1024 channel base. The data was then folded and reduced to 256 channels for analysis and display. The spectrometer was calibrated using alpha iron, which serves also as an isomer shift reference. A small impurity (max. absorption 0.17%) associated with iron in the beryllium window of the gas proportional counter was subtracted before analysis.

In situ X-ray absorption spectroscopy

In situ XANES measurements were performed at the QAS beamline (7-BM) at the National Synchrotron Light Source II (NSLS-II). The beamline operates with a 3-pole wiggler source, utilizing a 700 mm-long Rh-coated collimating mirror, followed by a water-cooled, channel-cut Si(111) crystal fly-scan monochromator. The beam is then focused using a 1000 mm-long Rh-coated toroidal mirror. At the sample position, the beam size is approximately 500 μm horizontal × 500 μm vertical. Harmonic rejection is achieved by detuning the monochromator with a pico-motor, which applies pressure to one side of the channel-cut crystal. We used a custom-designed 3-electrode aqueous cell with a Ni₈Fe catalyst/carbon paper working electrode, a carbon paper counter electrode positioned opposite the working electrode, and a mercury/mercury oxide reference electrode



calibrated with respect to the RHE in 0.1 M KOH (0.92 V vs. RHE). All potentials have been compensated for the electrolyte resistance using the built-in compensation function of the CH Instruments 760E potentiostat. Typical resistance values measured immediately preceding the X-ray data collection were 17 to 19 Ω . The 0.1 M KOH electrolyte was continuously flowed through the cell at a flow rate of 50 mL min⁻¹, through an inlet at the bottom of the cell and outlet at the top, using a peristaltic pump (NE-9000G). The XANES data were acquired in fluorescence mode at a 45° incidence angle using a silicon drift detector. Ni and Fe metal foils were measured in transmission mode before and after the *in situ* experiments for energy calibration. The experimental setup is shown in Fig. S2 and S3 (ESI†). An identical potential profile to that used for Mössbauer spectroscopy was applied for *in situ* XANES, except the dwell times were shorter for XANES (~20 min).

In situ EXAFS measurements were performed at beamline 10-ID, the Advanced Photon Source (APS), Argonne National Laboratory, operated by the Materials Research Collaborative Access Team (MR-CAT). The X-ray energy was selected using a liquid nitrogen cooled Si(111) double crystal monochromator with a bare silica (ULE glass) harmonic rejection mirror.⁴⁴ The undulator gap was scanned quasi-synchronously with the monochromator energy during the continuous energy scan (0.25 eV and 0.35 eV binning and 0.05 s and 0.03 s per bin for Fe and Ni spectra, respectively). Spectra were measured in fluorescence mode and without filters to allow rapid switching between the Fe and Ni K edges. Spectra were acquired from 1.0 V to 1.7 V in varying potential steps for both increasing and decreasing potential profiles. A different potential profile was used for EXAFS measurements compared to the XANES and Mössbauer measurements, but comparison of the EXAFS regions of the data acquired at the two beamlines and with different potential profiles were consistent (Fig. S8, ESI†). All potentials have been compensated for the resistance of the electrolyte, corrected using the built-in compensation function of the CH Instruments 760D potentiostat. The acquisition time for each EXAFS scan was approximately 2 minutes and spectra were acquired at any given potential until two consecutive spectra were identical.

All XANES and EXAFS spectra were normalized using the Athena software program.⁴⁵ The EXAFS spectra were fit using Artemis.⁴⁵ K-windows of 3–13 Å⁻¹ and 3–12.7 Å⁻¹ were applied to the Fourier transforms of Fe and Ni K-edge spectra, respectively, and fitting windows of 1–3 Å were used to capture the first and second coordination shells. We fit an α -Ni(OH)₂ standard material (Fig. S9, ESI†) as a reference to monitor the fit Debye–Waller factors for sample spectra; if sample values were within error of the reference value, they were fixed to match the reference to decrease uncertainty and increase comparability of coordination numbers. To partially account for the non-self-consistent field scattering path calculations (feff version 6), the relative energy shifts applied to the Ni–O and Ni–Ni paths were constrained to be the same as that found for Ni(OH)₂ (i.e., $\Delta E_{0(\text{Ni-M})} = \Delta E_{0(\text{Ni-O})} + 4.17$ eV). This correction was only made for the Ni K edge fits, due to the lack of an

appropriate empirical standard for the Fe K edge (e.g., Fe-doped Ni(OH)₂). Due to the similar electron densities of Ni and Fe, EXAFS cannot distinguish between the two scatterers in the second shell scattering paths of Fe or Ni. The Fe and Ni K-edge EXAFS second shell scattering paths were thus fit using Ni in the second shell.

Scanning transmission electron microscopy

Specimens from catalyst-coated carbon paper were sonicated in isopropanol to form a dispersion, then drop-cast onto a copper TEM grid. High-angle annular dark-field scanning transmission electron microscopy (HAADF-STEM) images, energy-dispersive X-ray spectroscopy (EDS), and electron energy-loss spectroscopy (EELS) were recorded using an aberration-corrected JEM-ARM200F “NEOARM” analytical electron microscope (JEOL Ltd.). The microscope was operated at 200 kV and equipped with dual windowless silicon-drift detectors (SDD) each with a 100 mm² active area. The EDS data were processed using Analysis Station (JEOL Ltd.) software. EELS data were recorded using Gatan Digital Micrograph (Gatan Inc.) and processed using a custom Python code to measure the thickness of the specimen.

Results and discussion

In situ ⁵⁷Fe Mössbauer spectroscopy

The cell currents recorded during each of the potentiostatic holds of the *in situ* Mössbauer experiments are shown in Fig. 2a. Currents recorded at ≥ 1.55 V show pronounced noise due to an increased rate of oxygen bubble evolution on the electrode surface followed by bubble detachment, facilitated by electrolyte circulation. The current recorded over the last 2 hours of the step was averaged to represent the steady-state current at each potential (Fig. 2c (in red)). The full current–time profile can be found in Fig. S4 (ESI†). Fig. 2b shows the cyclic voltammetry (CV, measured at 10 mV s⁻¹) and the staircase voltammetry (SV, 10 mV steps, 10 s holds, reported current at the end of 10 s) measured with a rotating disk electrode (RDE), as described in Osmieri *et al.*⁴¹ The voltametric peak during the positive-going potential sweep has been attributed to Ni(II) oxidation in the literature.^{14,46,47} Comparison of this voltammetric feature with the onset of OER in the SV shows that the onset of OER at ~1.45 V is coincident with a decrease in the current associated with Ni(II) oxidation. The onset potential for OER measured during the *in situ* Fe MS experiment is also ~1.45 V (Fig. 2c), in agreement with both the SV shown here and in Osmieri *et al.*⁴¹

For the *in situ* Fe MS experiment, the steady-state current increases monotonically as the potential increases to 1.75 V and decreases as the potential decreases (Fig. 2c). A small hysteresis is observed, with currents at any given potential slightly higher during the increasing potential profile than during the decreasing potential profile. This may be attributed to oxygen bubble accumulation on the electrode surface.⁴¹ Mössbauer spectra at a few selected potentials are displayed in Fig. 2a to illustrate the



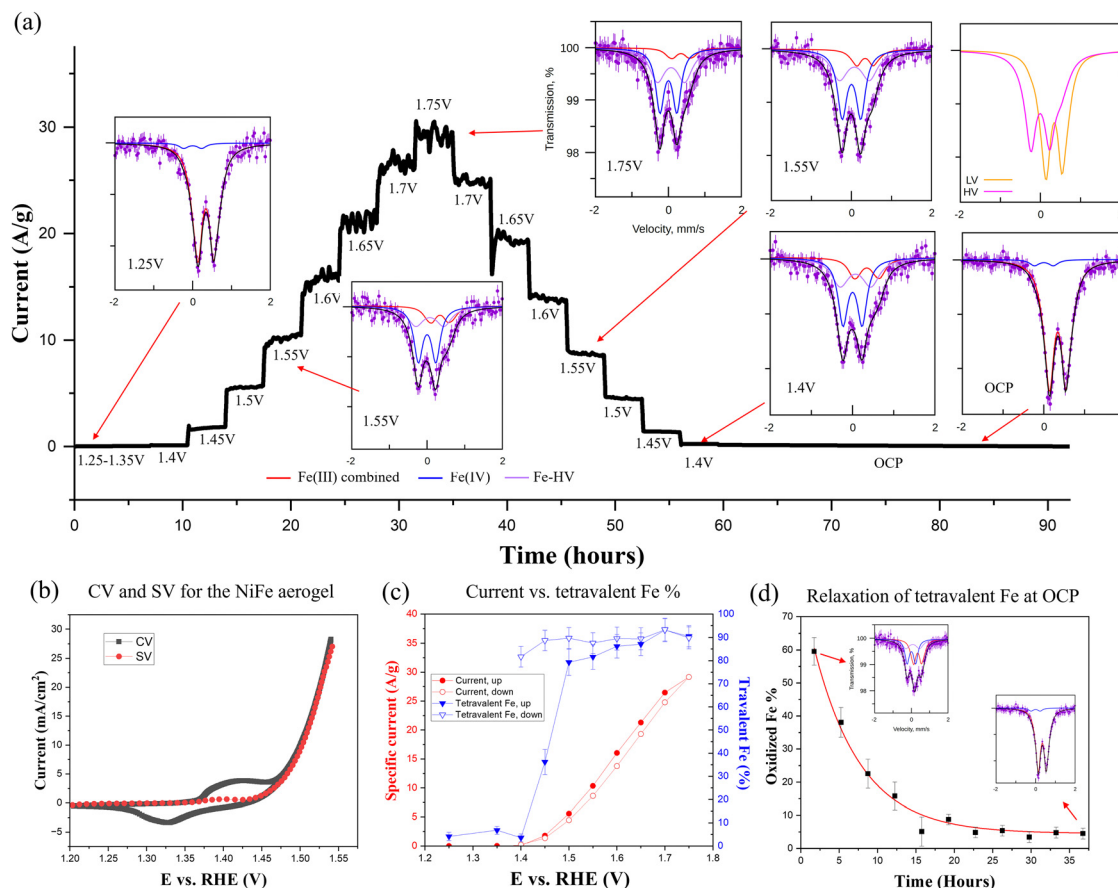


Fig. 2 (a) Mössbauer spectra at different potentials overlaid with the current measured during chronoamperometry. Three components are shown for each spectrum: Fe(IV) as blue, Fe-HV as purple, and Fe(III) as red (combining two Fe(III) species). Fitted spectra at low potential (orange) and high potential (magenta) are compared in the upper right corner showing the dramatic shift. For all Mössbauer spectra, the x-axis is velocity in mm s^{-1} and the y-axis is relative absorption, with 1% per tick mark. (b) Cyclic voltammogram (CV) and staircase voltammogram (SV) for the Ni_3Fe aerogel based on the data from our previous work.⁴¹ (c) An overlay of specific current at different potentials and the corresponding content of tetraivalent Fe content derived from Mössbauer spectra. (d) The amount of tetraivalent Fe as a function of time spent at OCP after chronoamperometric holds were completed. Two Mössbauer spectra are displayed for data at 2.5 hours and 33 hours. The potentials in (b) have been iR -corrected.

change of spectral shape and corresponding Fe species during the experiment. To identify the Fe species and spectral components, we combined Mössbauer spectra with the same shape. Spectra recorded at low potentials (1.25–1.40 V) represents Fe in a low oxidation state. Spectra recorded at ≥ 1.55 V in the positive-going potential profile and ≥ 1.40 V in the negative-going potential profile represent Fe in a high oxidation state. These combined spectra with high signal-to-noise ratios are shown in Fig. S5 (ESI ‡). At a minimum, four spectral components, and thus species, were identified with two attributable to Fe(III), one narrow component attributable to Fe(IV), and an additional high-valent Fe (referred to as Fe-HV) component that is slightly broader than that of Fe(IV). We refer to the latter two features generally as “tetraivalent” Fe and combined their contribution relative to the total amount of Fe throughout the discussion. For clarity, in Fig. 2 and later in Fig. 3, the two Fe(III) species are represented as one component (in red).

The fits of all spectra were consequently carried out as a principal-component analysis, where all spectral parameters of the four components were fixed, and only the relative amounts

and total spectral area were fit. Detailed fitting parameters for four Fe species in the Mössbauer spectra are shown in Table 1. The two Fe(III) species have similar isomer shifts (IS) but different quadrupole splitting (QS). The Fe(IV) component has an IS of ~ 0 and QS of 0.47 mm s^{-1} . The additional high-valent Fe-HV has a slightly different isomer shift of 0.07 and a QS of 0.75 mm s^{-1} . Both the quadrupole splitting and peak width of this type of Fe are larger than that noted for the Fe(IV) species. Spectra at each potential step were fit with these components; the results of these fits are summarized in Fig. 2a. Unlike Chen *et al.*³⁷ and Kuang *et al.*,³⁸ where a singlet was used for Fe(IV), the Mössbauer spectra in this work clearly exhibit a doublet feature at high potentials. This difference could be related to the much larger relative amount of tetraivalent iron observed here.

A typical IS for Fe(IV) is 0.082 mm s^{-1} reported by Wattiaux *et al.* for SrFeO_3 cubic perovskite prepared by electrochemical treatment.⁴⁸ But as expected for a highly symmetric iron environment, Wattiaux *et al.* reported a single peak with no QS.⁴⁸ The measured IS of Fe(IV) in the present work agrees well



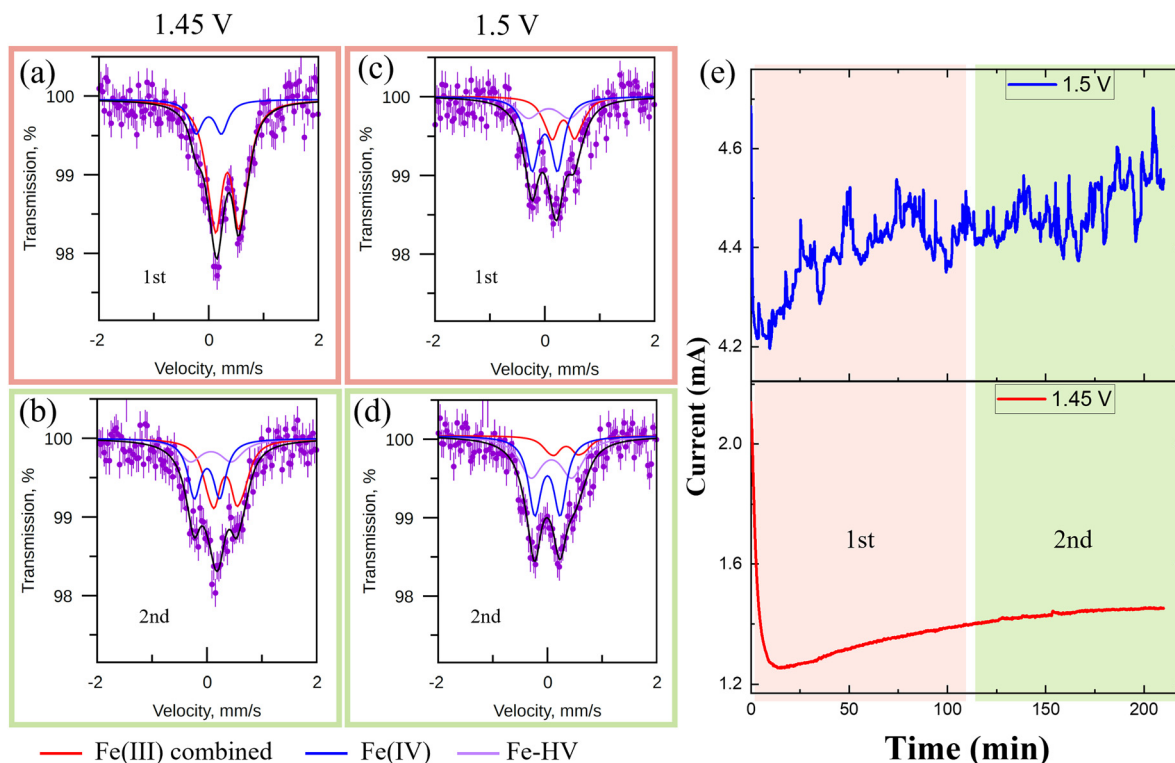


Fig. 3 The transition from Fe(III) to tetravalent Fe near the OER onset potential: (a) and (b) and (c) and (d) Mössbauer spectra from the 1st and 2nd half of the 3.5 h potential holds at 1.45 V and 1.5 V, respectively. Fe species colored as in Fig. 2. (e) Chronopotentiometry at potentials near the OER onset.

Table 1 Principal-component parameters for Mössbauer spectra. Unit: mm s^{-1}

	IS	QS	FWHM
Fe(IV)	0.001(3)	0.465(8)	0.284
Fe-HV	0.07(1)	0.75(3)	0.505
Fe(III)A	0.338(3)	0.388(8)	0.250
Fe(III)B	0.349(7)	0.64(4)	0.348

IS: isomer shift; QS: quadrupole splitting; FWHM: the full width at half maximum. Errors are shown in brackets.

with Guerlou-Demourgues *et al.*⁴⁹ who also showed a doublet feature with QS of $0.38\text{--}0.56 \text{ mm s}^{-1}$ and IS of 0.01 mm s^{-1} . The slightly higher IS for Fe-HV may be attributed to fast electron hopping between Fe(III) and Fe(IV) sites, as argued in Guerlou-Demourgues *et al.*,⁴⁹ where a component with IS of 0.15 mm s^{-1} was interpreted as an average Fe valence of +3.5. The Fe(III) species have comparable IS with Chen *et al.*,³⁷ Kuang *et al.*,³⁸ Guerlou-Demourgues *et al.*,⁴⁹ and Kamnev *et al.*⁵⁰ Two distinctive QS for Fe(III) were also observed, which is comparable to Kamnev *et al.*,⁵⁰ where Fe(III) in Ni hydroxide shows a higher QS of 0.67 mm s^{-1} and Fe(III) in Ni oxyhydroxide shows a lower QS of 0.39 mm s^{-1} .

The majority of Fe at 1.25 V was present as Fe(III) with only $\sim 5\%$ of tetravalent Fe (only in the Fe(IV) form, similar to that reported in our analysis of the pristine catalyst powder⁴¹). The tetravalent Fe remained stable until 1.40 V, followed by a rapid increase at 1.45 V. Note that this rapid increase in tetravalent Fe

content coincides with the onset of OER. A plateau was reached at 1.50 V where $\sim 80\%$ of Fe was identified as tetravalent Fe, including 44% contributed by Fe(IV) and 36% by Fe-HV. Further potential increase resulted only in a minor increase in tetravalent Fe content from $\sim 80\%$ to $\sim 90\%$ (at 1.75 V). Although the OER current continued to increase above 1.45 V, the tetravalent Fe content increased only slightly. Interestingly, the plateau of tetravalent Fe content was not observed by Chen *et al.* or Kuang *et al.*^{37,38} Both studies show an increase in Fe(IV) content from the onset potential of OER to the highest potential in their respective experiments. When the OER current decreased in the decreasing potential portion of the profile, the amount of tetravalent Fe remained high at *ca.* 80–90% until the conclusion of the experiment at 1.40 V (Fig. 2c). A similar observation was reported by Chen *et al.*,³⁷ where Fe(IV) remained observable at the end of the experiment. To view relaxation of tetravalent Fe, we continued to record Mössbauer spectra for $\sim 35 \text{ h}$ at open circuit after the potential step profile (Fig. 2d). The half-life of tetravalent Fe in the electrode was found to be approximately 5 h and its content slowly dropped to below 10% after 24 h at open circuit, similar content to that found before the potential step profile ($\sim 5\%$) (Fig. 2c). Note that Kuang *et al.*³⁸ described that Fe(IV) completely disappeared after removing the applied potential without observation of such relaxation. A systematic comparison of experimental conditions and main observations of Chen *et al.*,³⁷ Kuang *et al.*,³⁸ and this work is shown

in Table S1 (ESI[†]). Different synthesis methodologies resulted in different structures and thus different Fe redox behavior at OER potentials. Higher crystallinity materials, as in Chen *et al.*³⁷ and Kuang *et al.*,³⁸ show lesser extent of conversion from Fe(III) to Fe(IV). Furthermore, the tetravalent Fe species shows a different isomer shift in MS, suggesting a different environment for Fe during OER. Only the aerogel catalyst showed a doublet, whereas materials with higher crystallinity showed a singlet.

A close examination of the transition from Fe(III) to Fe(IV) near the OER onset potential is shown in Fig. 3. Mössbauer spectra at 1.45 V and 1.50 V were averaged over the first and last 1.75-hour periods and these averaged spectra are displayed in Fig. 3a–d. A clear increase of Fe(IV) and emerging Fe–HV species can be observed by comparing the spectra acquired during the first and second half of the potential hold at 1.45 V. At 1.50 V, the Fe(III) component further decreased especially during the second half of the potential hold. The current–time responses at 1.45 and 1.50 V are shown in Fig. 3e. At both potentials, the current starts to rise after the initial decrease. The slow evolution of the formation of the tetravalent Fe species near the OER onset potential suggests that a major portion of the Fe may be oxidized in a diffusion-controlled process during the potential holds at 1.45 and 1.50 V. Eventually, the majority of Fe in the bulk of the catalyst is tetravalent at potential higher than 1.50 V. The slow increase in current may also be a consequence of this diffusion-controlled process. Note that the diffusion-controlled process is postulated qualitatively based on trends observed in the data. Validating this hypothesis would require constructing a model Ni/Fe hydroxide system which is beyond the scope of this work.

In situ X-ray absorption spectroscopy

To gain additional perspective on the chemical states of Ni and Fe under OER conditions, we performed *in situ* XAS at the Ni

and Fe K-edges following the same testing procedure as was used for *in situ* Mössbauer spectroscopy experiments, with the noted caveat that the potential steps were an order of magnitude shorter in duration, approximately 20 minutes. In the XANES region of the Ni K-edge, we observe an abrupt increase in the energy of both the absorption edge and the white line as the applied potential is increased from 1.4 to 1.45 V, indicative of Ni oxidation (Fig. 4a). The presence of an isosbestic point at *ca.* 8352 eV suggests that the spectra at any given potential comprise the sum of two unique components representing the original and oxidized species. Therefore, to more clearly represent the oxidation of Ni as a function of potential, we performed linear combination fits (LCFs) on each spectrum using the vertex potential spectra (1.25 and 1.75 V) as the fitting standards (Fig. 4b). This analysis was conducted with duplicate samples for the increasing and decreasing potential steps (data in black and red, respectively). From this analysis, we clearly observe the rapid and near complete transition of Ni to its oxidized form between 1.40 and 1.50 V, followed by the return to its original state between 1.45 and 1.30 V in the subsequent decreasing potential steps. These potential ranges are in good agreement with the potential ranges of the anodic and cathodic peaks, respectively, shown in the cyclic voltammogram in Fig. 2b.

Similarly, we observe a transition in the Fe K-edge XAS spectra at potentials above 1.40 V, evident by the slight increase in white line energy and decrease in white line intensity (Fig. 4d). Based on the *in situ* Mössbauer analysis described earlier and previous literature,^{16,21,36–40} we ascribe these changes to oxidation of Fe(III) to Fe(IV). The suppression of white line intensity concomitant with an increase in edge energy less than that expected based on lower valence state transitions (*e.g.*, shift of 3.84 eV per charge for Fe(II) to Fe(III)) has been previously attributed to an increase in the covalency of

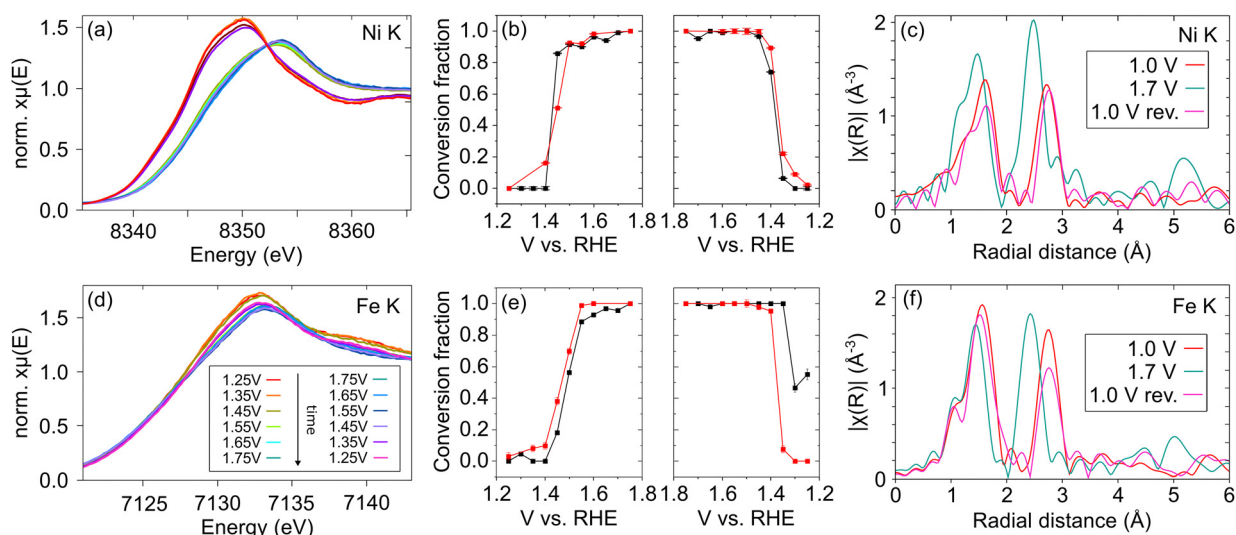


Fig. 4 *In situ* XANES spectra vs. applied bias at the (a) Ni K- and (d) Fe K-edges, with associated linear combination fits between endpoint spectra in (b) and (e), respectively, where black and red data are from fitting of spectra measured for duplicate samples. Fourier-transformed *in situ* EXAFS signal of (c) Ni K- and (f) Fe K-edge signals at vertex potentials.



the Fe–O bond resulting in oxygen to metal charge transfer, as is observed for Fe(IV) in lanthanum strontium iron perovskites.^{36,51,52} We also observe an increased intensity of the Fe K pre-edge feature at high potentials (Fig. S7, ESI†), as reported for the aforementioned perovskites,⁵¹ further supporting the presence of Fe(IV). LCF analysis reveals that Fe oxidizes between 1.40 and 1.55 V (Fig. 4e). At potentials > 1.55 V, further changes to the oxidation state of Fe are minimal, corroborating the *in situ* MS data. With decreasing potential, we observe different behavior for the two samples tested. Whereas one sample (in red) exhibited Fe reduction back to Fe(III) from 1.40 V to 1.30 V, the second sample (in black) did not fully return to Fe(III) during the test, adding further evidence for the propensity of Fe(IV) to linger in the Ni₈Fe hydroxide catalyst following exposure to OER potentials.

In addition to the chemical information provided by analysis of the XANES region, we also examined the effect of potential on the extended X-ray absorption fine structure (EXAFS), which reveals the local coordination structure of the Ni and Fe. At 1.0 V, the Fourier-transformed EXAFS spectra at the Ni and Fe K-edges (red lines in Fig. 4c and f) both reflect the structure of α -Ni(OH)₂ (Fig. S9, ESI†) with peaks at ~ 1.6 and 2.75 Å corresponding to M–O and M–Ni scattering paths, respectively, where M is the Ni or Fe absorbing atom. This indicates that Fe is predominantly incorporated into the α -Ni(OH)₂ structure rather than segregated into an additional Fe-containing phase, in agreement with the EDS data. More

detailed information is extracted by fitting the EXAFS spectra, the results of which are shown in Table 2 and Fig. S10 (ESI†). We note that only Ni was used in the fits of the second nearest neighbor scattering for both the Ni and Fe EXAFS data because Fe and Ni are not distinguishable due to their similar atomic numbers. However, this does not preclude possible Fe–Fe and Ni–Fe coordination within the Ni hydroxide and oxyhydroxide structures. While the Fe atoms appear to be nearly fully coordinated, with Fe–O and Fe–Ni coordination of 5.3 ± 0.6 and 5.6 ± 0.5 , respectively, Ni appears to be under-coordinated, with fit values of 4.5 ± 0.2 and 4.5 ± 0.3 for Ni–O and Ni–Ni, respectively. The under-coordination of Ni agrees with the XPS analysis from our previous work⁴¹ where a Ni/Fe ratio of 15.7 was found indicating surface enrichment of Ni. Additionally, whereas the Fe–O distance (2.009 ± 0.009 Å) is shorter than the Ni–O distance (2.045 ± 0.008 Å), the metal–metal distances appear to not depend on the identity of the scattering atom (3.101 ± 0.009 Å and 3.103 ± 0.007 Å for Fe and Ni, respectively), further suggesting that the minority Fe atoms are incorporated into α -Ni(OH)₂. These Fe–O and Ni–O distances are comparable to the distances of 2.01 Å and 2.06 Å, respectively, observed by Friebe *et al.*²⁹ for an electrodeposited Ni₃Fe oxyhydroxide thin film polarized at 1.12 V.

Upon applying a potential of 1.7 V (plotted in teal in Fig. 4c and f), we observe contraction of all scattering paths, consistent with further oxidation of the metal observed *via* Mössbauer spectroscopy (in the case of Fe) and with the XANES analysis.

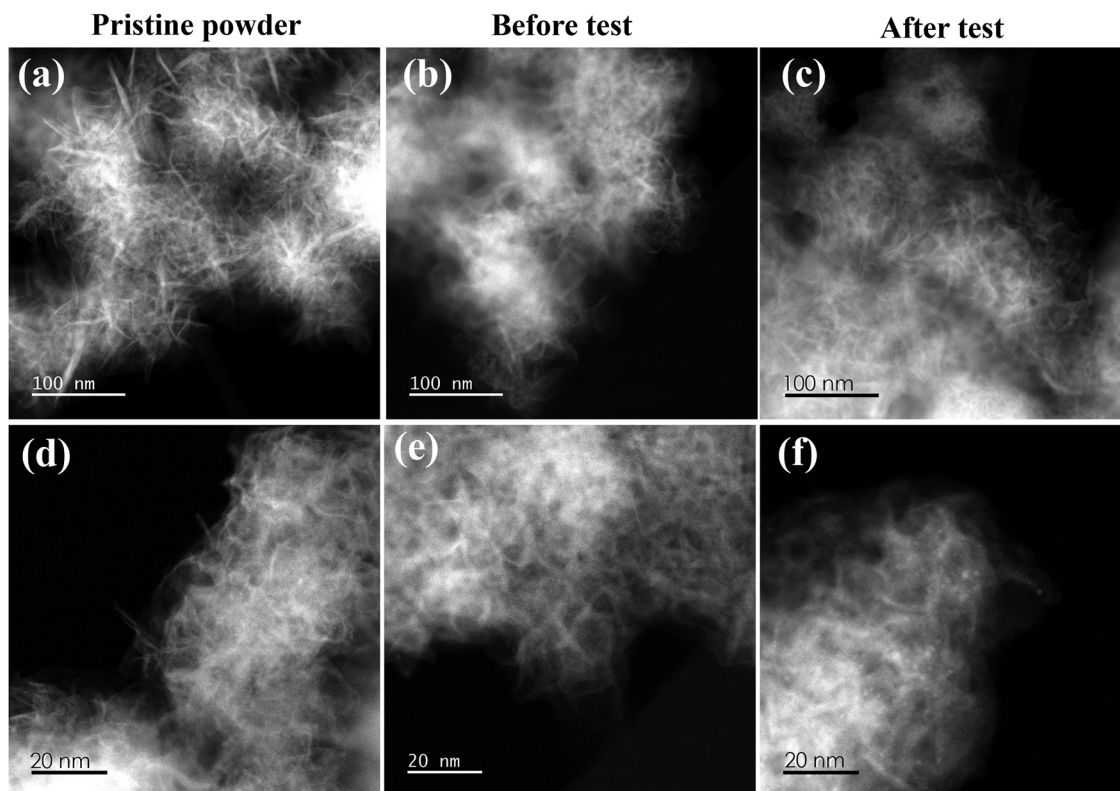


Fig. 5 The morphology of Ni₈Fe aerogel catalyst imaged using HAADF-STEM as (a) and (d) pristine powder, (b) and (e) before the *in situ* MS test, and (c) and (f) after the *in situ* MS test.



Table 2 Results from fitting of Fe K-edge and Ni K-edge *in situ* EXAFS data using Artemis.⁴⁵ Note that separate energy correction factors (ΔE_0) were used for Ni K-edge fits to account for the lack of self-consistent potentials in FEFF6, see Experimental section. Ni K-edge spectra from 1.60, 1.65, and 1.70 V were merged to improve signal-to-noise. All second nearest neighbor paths were fit using Ni as the scattering atom, though we do not exclude the possibility of Fe–Fe coordination and Ni–Fe coordination

	Applied potential vs. RHE	R-factor	Path	ΔE_0 (eV)	Coord. no.	Path length (Å)	σ^2 (Å ²)
Fe K edge	1.0 V	0.0144	Fe–O	-2.1 ± 1.1	5.3 ± 0.6	2.009 ± 0.009	0.0043 ± 0.0014
			Fe–Ni		5.6 ± 0.5	3.101 ± 0.009	0.0064^a
	1.7 V	0.0149	Fe–O	-0.7 ± 1.0	4.8 ± 0.2	1.904 ± 0.008	0.0054^a
			Fe–Ni		4.9 ± 0.4	2.845 ± 0.008	0.0050 ± 0.0012
Ni K edge	1.0 V	0.0089	Ni–O	$E_{O,1} = -3.7 \pm 0.8$	4.5 ± 0.2	2.045 ± 0.008	0.0054^a
			Ni–Ni	$E_{O,1} + 4.2$	4.5 ± 0.3	3.103 ± 0.007	0.0064^a
	1.6–1.7 V	0.0182	Ni–O	$E_{O,2} = -4.5 \pm 1.6$	4.3 ± 0.4	1.879 ± 0.013	0.0054^a
			Ni–Ni	$E_{O,2} + 4.2$	3.1 ± 0.7	2.830 ± 0.010	0.0025 ± 0.0014

^a Debye–Waller factors (σ^2) that did not significantly deviate from values obtained in the Ni(OH)₂ fit (0.0054 and 0.0064 for M–O and M–Ni, respectively) were not fit. All second nearest neighbor paths were fit using Ni as the scattering atom, but we do not exclude the possibility of Fe–Fe coordination.

From EXAFS fitting, we calculate these distances to be consistent with γ -NiOOH based on reported crystallographic data.⁵³ This phase is known to contain intercalated water and ions which are not included in the chemical formula,^{54,55} which result in an average oxidation state between (III) and (IV).^{56–58} Similar to what was observed at 1.0 V, the metal–metal distances are highly similar across scattering atoms (2.845 ± 0.008 Å and 2.83 ± 0.01 Å for Fe and Ni, respectively), indicating that Fe atoms are incorporated into γ -NiOOH rather than being located between NiOOH sheets, segregated into an additional phase, or on the surface of γ -NiOOH crystallites. The observed Fe–O bond length of 1.904 Å is comparable to that reported by Haas *et al.*⁵¹ for SrFeO_{3– δ} (1.9021 Å) and is indicative of a large fraction of the Fe being converted to Fe(IV) at this potential.⁵² Friebe *et al.*²⁹ reported an identical Fe–O bond length for their Ni₃Fe oxyhydroxide thin film polarized at 1.62 V vs. RHE (1.90 Å). Unlike Balasubramanian *et al.*,³⁶ however, Friebe *et al.*²⁹ and Halldin Stenlid *et al.*³⁵ attributed the slight changes in the Fe edge energy upon polarization to OER potentials to contraction of the Fe–O bond, not to changes in the oxidation state of Fe from Fe(III) to Fe(IV), based on the lack of a substantial increase in edge energy. Rather, Friebe *et al.*²⁹ attribute their experimental observations to changes in the 4p unoccupied pDOS with potential and Halldin Stenlid *et al.*³⁵ to changes in Fe coordination geometry from O_h to C_{4v} and increased covalency of the Fe–O bond. The Mössbauer data presented earlier definitively show the oxidation of Fe(III) to Fe(IV) at OER potentials, supporting the interpretation of Balasubramanian *et al.*³⁶ of Fe(IV) formation causing Fe–O bond contraction. Also, where Friebe *et al.*²⁹ observe a decrease in coordination number of ~ 1 for the Ni₃Fe electrodeposited thin film when

transitioning from 1.12 V to 1.62 V, we do not observe a significant change in coordination numbers with potential (*i.e.*, the error bars at 1.0 and 1.7 V overlap).

Based on the above discussions, *in situ* EXAFS measurements indicate a clear phase transformation from α -Ni(OH)₂ to γ -NiOOH during OER. The primary evidence for this phase transition in the EXAFS data lies in the contraction of the metal–metal scattering path (second nearest neighbor), which is more reflective of crystal structure than the metal–oxygen (first nearest neighbor) path since the metal–oxygen path is strongly influenced by the metal's oxidation state. Below OER potentials, the Ni–M path length is 3.103 ± 0.007 Å, consistent with literature for α -Ni(OH)₂.^{35,59,60} At OER potentials, the Ni–M path length is 2.83 ± 0.01 Å, consistent with γ -NiOOH.^{35,54,59}

The oxidation state of Ni and Fe at 1.0 V and 1.7 V can be estimated by comparing the bond lengths derived from the EXAFS fits to those of Ni and Fe standards with known oxidation states.²⁹ The calculated fractions of Fe(III), Fe(IV), Ni(II), Ni(III), and Ni(IV) are shown in Table 3 using the bond lengths compiled by Friebe *et al.*²⁹ for the indicated standard Ni and Fe compounds. The MS fractions of Fe(III) and tetravalent Fe are shown for comparison. This analysis shows that nearly all the Fe(III) present at 1.0 V, comprising 94% of the total Fe, is converted to Fe(IV) at 1.7 V, consistent with the MS results. This analysis also shows that all the Ni is Ni(II) at 1.0 V and that 92% of the Ni(II) is converted to the mixed III/IV oxidation state of γ -NiOOH at 1.7 V, consistent with the Ni XANES data.

Bond lengths (except where noted) from Friebe *et al.*:²⁹ α -FeOOH: 2.014 Å; SrFeO₃ (Haas *et al.*⁵¹): 1.902 Å; α -Ni(OH)₂: 2.042 Å; γ -NiOOH: 1.882 Å.

Table 3 Calculated fractions of Fe(III), Fe(IV), Ni(II), Ni(III), and Ni(IV) as a function of potential based on metal–oxygen bond lengths derived from EXAFS data. Fractions of Fe species from *in situ* Mössbauer (MS) data fits are shown for comparison

	Fe ³⁺ (α -FeOOH)	Fe ⁴⁺ average (SrFeO ₃)	Average Fe ox.	Ni ²⁺ (α -Ni(OH) ₂)	33% Ni ³⁺ /67% Ni ⁴⁺ (γ -NiOOH)	Average Ni ox.
XAS 1.0 V	0.94	0.06	3.06	1	0	2
XAS 1.7 V	0.02	0.98	4	0.08	0.92	3.54
MS 1.25 V	0.95	0.05	3.05			
MS > 1.55 V	0.11	0.89	3.89			



The EXAFS data acquired when decreasing the potential back to 1.0 V after polarization at 1.75 V, denoted “rev.”, were analyzed to evaluate reversibility of the observed changes in the coordination environment. LCF was performed for both the Fe and Ni K edge k^2 -weighted EXAFS spectra [$\chi(k)$]. The 1.0 V and 1.7 V spectra acquired during the increasing potential profile were used as components of the LCF for the spectrum acquired after returning to 1.0 V (Fe 1.0 V rev.). In the EXAFS experiments, the Fe returned substantially to the initial 1.0 V condition, but LCF analysis showed that $17\% \pm 2\%$ of the 1.7 V component remained (see Fig. S11, ESI†). At the Ni edge an average of the high potential spectra (1.6 V, 1.7 V, and 1.65 V rev.) was used as the nominal 1.7 V component to reduce the experimental noise. LCF of the Ni 1.0 rev. spectrum resulted in a best fit of $15\% \pm 2\%$ of the 1.7 V and 85% of the initial 1.0 V spectra. These data illustrate the slow kinetics of the evolution of the Fe-doped γ -NiOOH back to the Fe-doped α -Ni(OH)₂ structure, similar to what was observed in both the MS and XANES experiments.²⁹

The Ni₈Fe catalyst appears to be structurally reversible based on the final MS and XAS spectra being similar to those for the initial state. The MS at 1.25 V and at OCP after testing are almost identical as shown in Fig. 2 and Fig. S13 (in Note S1, ESI†), suggesting that Fe returns to its original state after ~30 hours at OCP, with a half-life of ~5 hours. For XAS, Fig. 4 and Fig. S11 (ESI†) show that the Ni and Fe XANES and EXAFS, respectively, are reversible. Visually, the catalyst coating on the carbon paper also returns to its original yellow color after being dried in ambient air (enclosed in a sample bag).

Morphology, composition, and surface area of Ni₈Fe aerogel

To further understand the electrochemical and potential-dependent Fe speciation, HAADF-STEM images were acquired for the pristine Ni₈Fe aerogel powder and the catalyst layer before and after the *in situ* MS tests. Fig. 5 shows representative HAADF-STEM images. The general morphology of the catalyst is typical of Ni hydroxide comprised of thin sheets and is qualitatively comparable at different stages of the *in situ* MS experiment. The energy dispersive X-ray spectroscopy (EDS) results confirm that the Ni-to-Fe ratio and metal-to-oxygen ratio are comparable before and after the *in situ* Mössbauer experiment (Table 4). This indicates that the material is stable during *in situ* MS without major catalyst dissolution or structural modifications, giving confidence to the results from *in situ* MS experiment. It also correlates with the absence of area loss

in MS before and after testing (Fig. S13, ESI†). EDS maps shown in Fig. S6 (ESI†) suggest no phase segregation of Ni and Fe.

The amount of electrochemically accessible catalytic sites during OER may be correlated with surface area, pore structure, and crystallite size. These factors combined may contribute to a larger fraction of Fe in the system being electrochemically accessible and able to be readily converted to a higher oxidation state during polarization at OER potentials. To further understand and illustrate the structure and dimensions of the Ni₈Fe aerogel nanosheets, STEM-EELS mapping was performed on the catalyst powder. Fig. S12 (ESI†) displays two representative areas where STEM-EELS maps were acquired. The absolute thickness of the material can be estimated using STEM-EELS as introduced in Malis *et al.*⁶¹ Using eqn (7) in Malis *et al.*⁶¹ with an electron energy (200 keV) and a convergence angle (28 mrad) used in present work, the electron mean free path is approx. 93 nm (based on atomic compositions in Table 4). Thus, absolute thickness of 5–9 nm can be estimated based on Fig. S12e and f (ESI†) with t/λ being about 0.05–0.1 in the thin edge areas. The high resolution imaging and EELS analysis show that the Ni₈Fe aerogel consists of thin sheets of NiFe oxide/hydroxide that are just a few nanometers thick. Such nanosheet morphology for the Ni₈Fe aerogel is commonly observed during STEM imaging for the present work and in Osmieri *et al.*⁴¹ Using the maximum estimated thickness of 90 Å of the nanosheets and the average interlayer spacing reported in the literature for α -NiFe layered double hydroxide of 8 Å,⁶² the number of Ni₈Fe layers in a typical nanosheet of the Ni₈Fe aerogel is approximately 11. Based on this estimate, 2/11 or 18% of the NiFe oxyhydroxide sites are on the surface of the nanosheets and exposed directly to the aqueous electrolyte, neglecting the NiFe sites at the edges of the layers which represent a small fraction of the total number of sites.

The Ni₈Fe aerogel catalyst analyzed in the present work has a very high Brunauer–Emmett–Teller (BET) surface area of 382 m² g^{−1} measured using N₂ adsorption.⁴¹ The XRD pattern for this material in Osmieri *et al.*⁴¹ shows broad peaks suggesting an amorphous or nanocrystalline structure. In comparison, the porosity and BET surface area information for a NiFe-LDH synthesized by co-deposition was not reported in Chen *et al.*,³⁷ but the XRD pattern showed pronounced crystalline structure (resembling that of α -Ni(OH)₂) suggesting large crystallite size. The NiFe-LDH reported by Kuang *et al.*³⁸ displayed a structure with low crystallinity in the XRD pattern and an agglomerate size on the order of 200 nm from STEM images.

To assess the accessibility of the NiFe oxide/hydroxide sites with the Ni₈Fe nanosheets, the measured BET surface area of 382 m² g^{−1} was compared to the calculated area of the Ni_{0.88}Fe_{0.11}(OH)_x unit cell using the nominal oxidation states of Ni(II) and Fe(III) (*i.e.*, $x = 0.88 \times 2 + 0.11 \times 3$), a Ni(II) radius of 0.77 Å, and assuming octahedral coordination of each metal atom with OH, as observed in α -Ni(OH)₂.⁶³ This calculation yielded a unit cell area of 8.47 Å². The measured BET surface area, converted to area per Ni_{0.88}Fe_{0.11}(OH)_x unit cell using the nominal molecular weight of 93.47 g mol^{−1}, is 5.93 Å² per unit cell. The area of a unit cell and the BET area per unit cell are

Table 4 Elemental compositions based on five EDS maps. Errors are shown in parenthesis

Elements	Before test (at% or ratio)	After test (at% or ratio)
O	73(1)	73(3)
Fe	3.2(1)	3.2(4)
Ni	24(1)	24(3)
Ni/Fe ratio	7.7(3)	7.4(4)
Metal/oxygen ratio	0.38(2)	0.37(6)



comparable (8.47 \AA^2 vs. 5.93 \AA^2 per unit cell, respectively) indicating that that nearly all the NiFe oxide/hydroxide sites in the Ni_8Fe aerogel nanosheets are accessible to molecular nitrogen and not just the $\sim 18\%$ on the surface of the 90 \AA thick nanosheets.

We can now compare the charge in the redox features of the CV shown in Fig. 2b to the total number of Ni and Fe on the RDE tip to determine the percent of these sites that are oxidized and reduced in a voltametric sweep at 10 mV s^{-1} . This comparison, assuming for simplicity a one-electron transfer for both Fe and Ni, yields 11% of the total Ni and Fe atoms oxidized in the anodic wave and 12% reduced in the cathodic wave. These values are comparable to the estimate of 18% of NiFe sites on the surface of the nanosheets indicating that the redox features observed during a potentiodynamic sweep are attributable to surface metal atoms only. Both the *in situ* MS and XAS data show that potential holds of 3.5 h and $\sim 20\text{--}40 \text{ min}$ at 1.45 V, respectively, result in oxidation of 36.5% of Fe by MS, 18% Fe by XAS, and 86% Ni by XAS, whereas by 1.45 V in the positive-going CV, only $\sim 8\%$ of the total Ni and Fe have been oxidized. The differences between the extent of oxidation in a 10 mV s^{-1} CV *versus* those observed in long ($\geq 20 \text{ min}$) potential holds and the slow evolution of the formation of the tetravalent Fe species at ≥ 1.45 in the MS experiments indicate that the oxidation of Ni and Fe atoms beyond those located on the surfaces of the nanosheets (*i.e.*, in the bulk of the $\sim 90 \text{ \AA}$ thick nanosheets) is a slow process. Given the timescale of this oxidation, it is most likely controlled by diffusion of ions into the spaces between the NiFeO_x layers of the nanosheets. As discussed by Acharya *et al.*,⁶⁴ diffusion coefficients of ions into the bulk of $\alpha\text{-Ni}(\text{OH})_2$ have been estimated to be 10^{-9} to $10^{-12} \text{ cm}^2 \text{ s}^{-1}$ in the literature,^{65–70} with prior work assuming protons as the diffusing species.⁷⁰ Acharya *et al.*, however, concluded that the species diffusing into the bulk of the particles is OH^- rather than H^+ , based on the rate constant for Ni oxidation (0.00426 s^{-1}) derived from time-resolved *in situ* Ni XAS of NiFeO_x particles.⁶⁴ The gradual increase of tetravalent Fe in MS (Fig. 3a–d) over a period of $\sim 100 \text{ min}$ agrees with the

oxidation of Fe(III) to tetravalent Fe being a diffusion-controlled process. The OER current recorded during the MS measurement (Fig. 3e) increases over the same period as the catalyst transforms into a more active state with high-valent Ni and Fe species throughout the Ni_8Fe nanosheets.

Correlation of Ni and Fe redox and OER

Fig. 6 overlays the SV with the percentage of oxidized Ni and Fe as a function of potential, as determined using MS and XAS. The MS and XANES results show that the onset potential for OER correlates well with the potential at which both Ni and Fe are oxidized (1.45 V). For XAS, a majority of the Ni is oxidized between 1.4 and 1.45 V (89%), whereas only 18% of the Fe is oxidized, which may indicate that either Ni oxidation is necessary to initiate Fe oxidation or that only a minority of Fe needs to be oxidized to induce oxidation of Ni throughout the nanosheets. The high percentages Fe and Ni undergoing oxidation at $>1.5 \text{ V}$ (Table 3 and Fig. 6) indicate that electrical conductivity of the Ni_8Fe oxyhydroxide^{10,12,14,57} is not limiting either Ni and Fe oxidation or OER. Both Ni and Fe remain in high valence states at potentials higher than the OER onset (Fig. 6a and Table 3). As the potential is decreased (Fig. 6b), Ni begins to revert to its original oxidation state at approximately 50 mV lower than the OER onset potential, agreeing well with the potential range of the cathodic redox feature in the CV. The MS and XAS data show that a significant fraction of Fe remains in the high oxidation state during the entire cathodic-going potential profile.

Based on analysis of the *in situ* EXAFS data, at potentials below the onset of OER, Fe(III) is incorporated into Ni(II) oxide with an $\alpha\text{-Ni}(\text{OH})_2$ structure. The Fe–O bond in this structure is shorter than the Ni–O bond due to the higher oxidation state of Fe; this shorter bond distance can cause strain in the $\alpha\text{-Ni}(\text{OH})_2$ lattice. The Fe is closer to fully coordinated ($\text{CN} \sim 5.3$) than Ni ($\text{CN} \sim 4.5$), suggesting either that there exists a significant number of O and Ni vacancies primarily located near Ni, or that Ni is overrepresented at the surface of the nanosheets. The XPS data of Osmieri *et al.*⁴¹ support surface enrichment by Ni,

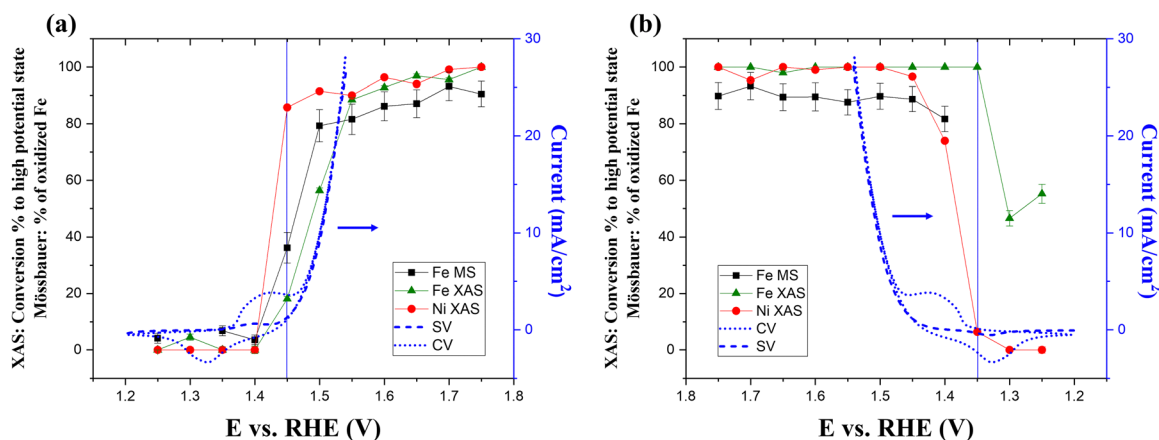


Fig. 6 Comparing the percent of oxidation species measured during *in situ* MS and XAS experiments with SV curves: (a) is the anodic scan and (b) is the cathodic scan.



showing a Ni-to-Fe atomic ratio of 15.7 in the near surface region of the as-prepared Ni₈Fe aerogel, double the overall ratio determined by EDS in this work (7.7, Table 4). Due to the small nanosheet size and high porosity of the catalyst, the undercoordinated surface Ni (18% of nanosheet area is estimated to be on the surface) would represent a significant fraction of the overall Ni in the catalyst. At OER potentials, Fe(III) is oxidized to Fe(IV), Ni(II) is oxidized, and the oxide adopts a γ -NiOOH structure, resulting in an average Ni oxidation state of ~ 3.5 and contraction of both the Fe–O and Ni–O bond distances (by 0.105 Å and 0.166 Å, respectively). In addition to contraction of the M–O bonds, the Fe XANES and pre-edge regions show evidence of increased covalency of the Fe–O bond and the Ni XANES also shows evidence of increased charge transfer into the Ni 4p orbitals.

The comparison of the CV, the change in valence state of Fe observed *via* Mössbauer and XAS, and the change in Ni oxidation state observed by XAS, as shown in Fig. 6, indicates that Ni and Fe are both oxidized at 1.45 V coinciding with the onset of OER and the near completion of the Ni oxidation feature in the CV. However, at 1.45 V, the XAS data show that the Ni has reached $\sim 88\%$ of the oxidation state reached at 1.75 V, but Fe has only reached ~ 20 to 40% of its 1.75 V oxidation state. Based on comparison of the CVs of the Ni₈Fe catalyst with CVs of Ni hydroxide aerogel synthesized using the same procedure (Fig. S14, ESI,† data from Osmieri *et al.*⁴¹), incorporation of Fe into the α -Ni(OH)₂ lattice increases the extent of Ni oxidation in the 1.38 V to 1.45 V potential range. The suppression of the XANES white line for the Ni₈Fe catalyst *versus* that for the α -Ni(OH)₂ standard (Fig. 7c of Osmieri *et al.*⁴¹) is indicative of increased occupancy of the Ni 4p orbitals induced by Fe in the α -Ni(OH)₂ lattice. The nearly complete conversion of Ni from 2+ in the α -Ni(OH)₂ structure to 3.5+ in the γ -NiOOH structure coincides with the onset potential of OER.

Turnover frequencies (TOF) at an OER overpotential of 300 mV (*i.e.*, at 1.53 V *vs.* RHE) based on the SV results (*i.e.*, with a 10 second hold time) are 0.77 s^{−1} normalized to all Fe sites in the catalyst, 0.024 s^{−1} normalized to all Ni sites in the catalyst, 3.4 s^{−1} normalized just to surface Fe (based on the anodic peak charge in the CV and the XPS Ni to Fe ratio of 15.7, *i.e.*, 6 mol% Fe), and 0.21 s^{−1} normalized just to surface Ni. The 3.4 s^{−1} calculated on a per surface Fe basis is comparable to the TOF of 3.1 s^{−1} reported by Klaus *et al.*³⁰ for a thin film of Ni(OH)₂/NiOOH deposited on Au and aged in Fe-containing 1 M KOH to achieve an Fe content of 6.8 mol% Fe (Fig. 12 of Klaus *et al.*³⁰). The comparability of the OER TOF normalized to surface Fe observed here and the TOF reported by Klaus *et al.* is further evidence that at short timescales (*i.e.*, seconds) Ni and Fe oxidation and OER are only occurring on the surface of the Ni₈Fe oxyhydroxide aerogel nanosheets.

In this work, we show strong correlations between the onset of OER current and the oxidation of Fe and Ni in the catalyst. The precise functions of Fe and Ni, however, are better interpreted through theoretical efforts, such as DFT modeling. Ahn *et al.*⁷¹ proposed that both Ni and Fe have two types of active sites, with one proposed to be Fe based on the match between

the fraction of fast OER sites from rate constants and the fraction of Fe in the catalyst. Ou *et al.*⁷² proposed that Fe–O–Fe dimers adsorbed on the surface of NiO_xH_y are the active sites and that Fe incorporated into the bulk of the NiO_xH_y is not OER active, only serving to withdraw electrons from Ni causing the observed anodic shift in the redox feature associated with the Ni(II) to Ni(III) transition. The following observations from our study argue against surface Fe being the dominant active site, for Fe being incorporated in the bulk of the γ -NiOOH structure, and for NiO_xH_y being the predominant surface species and thus the active site: (1) the lower M–O and M–Ni coordination for Ni than for Fe, implying undercoordination of Ni, (2) the much shorter Fe–O bond distances than those observed by Ou *et al.* for surface adsorbed Fe–O, and (3) MS and XAS show that the majority of the Fe remains in the higher oxidation state induced by polarization at OER potentials even when returning to potentials below the onset of OER. Theoretical work of Xiao *et al.*²¹ proposed that pure Ni sites are ineffective at producing O radicals, and that d⁴ Fe(IV) ions stabilize oxyl radical species formed on Ni(IV) sites through exchange interaction while the low spin d⁶ Ni(IV) ions promote the O–O coupling. More recently, theoretical work from Wang *et al.*²⁴ examines various pathways of O–O coupling mechanism and found that the LOM mechanism dominates the Ni-(oxy)hydroxides. Doping with Fe, however, greatly stabilizes adsorbed O radicals and quenches the radical character of lattice oxygen due to increased ionic nature of metal–oxygen bonds,²⁴ or high oxidation state of metals. This results in a more facile AEM at lower overpotentials and suppresses the LOM mechanism, thereby greatly enhancing the OER activity.²⁴ The coincidence of the onset of OER with the potential at which Fe(III) is oxidized to Fe(IV) and Ni(II) is oxidized to Ni(III)/Ni(IV) support the mechanism proposed by Goddard and co-workers:^{21,24} there is synergy between the Ni and Fe sites and both Ni and Fe in high oxidation states are needed to promote OER. Further theoretical work is required to better understand the Ni–Fe synergy on the NiFe aerogel catalyst.

Conclusions

In this work, we performed *in situ* MS and XAS experiments on a Ni₈Fe aerogel catalyst to elucidate the chemical states and crystalline structures during OER. We found that the onset of OER current correlates with the oxidation of Ni and Fe species in the catalyst. *In situ* MS showed that 80–90% of Fe were converted to tetravalent Fe at potentials above OER which is approximately twice the highest value reported in the literature. The oxidation of both Ni and Fe are also evidenced from *in situ* XAS experiments. Below the OER onset potential, Fe is incorporated into an α -Ni(OH)₂ structure and nearly fully coordinated, whereas Ni is undercoordinated likely due to surface enrichment of Ni confirmed by XPS.⁴¹ Above the OER onset potential, lattice contraction is observed for both Ni and Fe in agreement with formation of Fe-doped γ -NiOOH. After the catalyst was scanned cathodically to below the OER onset



potential, *in situ* MS shows that Fe slowly relaxed from its tetravalent state to Fe(III) over more than 24 hours at OCP, corroborated by *in situ* XAS which also shows a portion of the Fe sites remaining in the oxidized state after returning to 1.0 V. Physicochemical analysis suggest that the Ni₈Fe aerogel has a morphology of nanosheet with 5–9 nm thickness, corresponding to ~11 layers of (oxy)hydroxide which results in 18% of the material being exposed to the surface. The nanosheet morphology led to high surface area for the Ni₈Fe aerogel and a large fraction of Ni being on the surface of the nanosheets due to surface enrichment of Ni and undercoordination of Ni. More fully coordinated Fe suggests that Fe is mostly in bulk, but the high percent of conversion from Fe(III) to tetravalent Fe observed by MS and XAS indicates that all the Fe is electrochemically accessible over the timescale of the MS and XAS measurements, in line with observations on the nanosheet morphology. The slow oxidation of Fe and relaxation of tetravalent Fe suggests a diffusion-controlled redox process for the bulk of Fe in the aerogel catalyst, whereas agreement between the redox charge in the CV and the estimated surface Ni and Fe based on nanosheet morphology suggests that oxidation of surface Ni and Fe are facile. Results in this work highlight the importance of high-valent Ni and Fe species for OER activity. Although Fe in the bulk may not be the active center for OER, its proximity to the catalyst surface in this nanosheet-structured material, within a few atomic layers of the surface, contributes to the stabilization of the adsorption of intermediate species on Ni, as proposed by Xiao *et al.*²¹ We conclude that Ni and Fe exhibit synergy during OER and the unique nanomorphology of the Ni₈Fe aerogel catalyst studied here led to the high performance reported previously.^{41,42}

Author contributions

H. Y. performed *in situ* MS experiments and electron microscopy characterization, data analysis, and manuscript writing and revision. M. E. S., J. P., A. J. K., and D. J. M. performed *in situ* XANES and EXAFS measurements, XAS analysis and visualization, funding acquisition, and manuscript writing and revision. L. O. synthesized the catalyst, measured CV and SV data in RDE, performed electrochemical data analysis, and contributed to manuscript writing and revision. D. Y. and L. M. assisted with development of *in situ* XAS methodology and data acquisition. X. L. and A. S. worked on cell design and electrode preparation for the *in situ* MS experiments. D. A. C. was responsible for funding acquisition, conceptualization of the correlative *in situ* MS and STEM experiments, as well as manuscript editing. P. Z. was responsible for funding acquisition and manuscript revision. R. P. H. performed *in situ* MS experiments, data analysis, and manuscript writing and revision.

Data availability

The authors declare that the data supporting the findings of this study, within the paper and its ESI,† are available upon

request to the authors. Mössbauer spectroscopy data is available upon request to R. P. H. X-ray absorption spectroscopy data is available upon request to D. J. M. Electron microscopy data is available upon request to H. Y.

Conflicts of interest

The authors claim no conflicts of interest.

Acknowledgements

This work was performed in the ElectroCat Consortium (ElectroCat 2.0), supported by the U.S. Department of Energy, Office of Energy Efficiency and Renewable Energy, Hydrogen and Fuel Cell Technologies Office (technology managers David Peterson and McKenzie Hubert). This work was authored in part by Oak Ridge National Laboratory operated by UT-Battelle, LLC, under contract no. DE-AC05-00OR22725, by Argonne National Laboratory, a DOE Office of Science Laboratory managed by the UChicago Argonne, LLC under contract no. DE-AC-02-06CH11357, and by Los Alamos National Laboratory operated by Triad National Security, LLC under US DOE contract no. 89233218CNA000001. This research used resources of the National Synchrotron Light Source II; a U.S. Department of Energy (DOE) Office of Science User Facility operated for the DOE Office of Science by Brookhaven National Laboratory under Contract No. DE-SC0012704. This research used resources of the Advanced Photon Source (APS); a U.S. Department of Energy (DOE) Office of Science User Facility operated for the DOE Office of Science by Argonne National Laboratory under Contract No. DE-AC02-06CH11357. MRCAT operations at the APS are supported by the Department of Energy and MRCAT member institutions. Electron microscopy analysis was supported by the Center for Nanophase Materials Sciences (CNMS), which is a U.S. Department of Energy, Office of Science User Facility at Oak Ridge National Laboratory.

References

- 1 *Global Hydrogen Review 2024 – Analysis*. IEA. <https://www.iea.org/reports/global-hydrogen-review-2024> [Accessed 3rd December 2024].
- 2 B. N. D. van Haersma Buma, M. Peretto, Z. M. Matar and G. van de Kaa, Towards renewable hydrogen-based electrolysis: Alkaline vs. Proton Exchange Membrane, *Heliyon*, 2023, **9**(7), e17999, DOI: [10.1016/j.heliyon.2023.e17999](https://doi.org/10.1016/j.heliyon.2023.e17999).
- 3 K. Ayers, High efficiency PEM water electrolysis: enabled by advanced catalysts, membranes, and processes, *Curr. Opin. Chem. Eng.*, 2021, **33**, 100719, DOI: [10.1016/j.coche.2021.100719](https://doi.org/10.1016/j.coche.2021.100719).
- 4 S. M. Alia, Current research in low temperature proton exchange membrane-based electrolysis and a necessary shift in focus, *Curr. Opin. Chem. Eng.*, 2021, **33**, 100703, DOI: [10.1016/j.coche.2021.100703](https://doi.org/10.1016/j.coche.2021.100703).



- 5 R. Subbaraman, D. Tripkovic, K. C. Chang, D. Strmcnik, A. P. Paulikas and P. Hirunsit, *et al.*, Trends in activity for the water electrolyser reactions on 3d M(Ni,Co,Fe,Mn) hydr(oxy)oxide catalysts, *Nat. Mater.*, 2012, **11**(6), 550–557, DOI: [10.1038/nmat3313](https://doi.org/10.1038/nmat3313).
- 6 I. Vincent and D. Bessarabov, Low cost hydrogen production by anion exchange membrane electrolysis: A review, *Renewable Sustainable Energy Rev.*, 2018, **81**, 1690–1704, DOI: [10.1016/j.rser.2017.05.258](https://doi.org/10.1016/j.rser.2017.05.258).
- 7 C. Li and J. B. Baek, The promise of hydrogen production from alkaline anion exchange membrane electrolyzers, *Nano Energy*, 2021, **87**, 106162, DOI: [10.1016/j.nanoen.2021.106162](https://doi.org/10.1016/j.nanoen.2021.106162).
- 8 C. Santoro, A. Lavacchi, P. Mustarelli, V. Di Noto, L. Elbaz and D. R. Dekel, *et al.*, What is Next in Anion-Exchange Membrane Water Electrolyzers? Bottlenecks, Benefits, and Future, *ChemSusChem*, 2022, **15**(8), e202200027, DOI: [10.1002/cssc.202200027](https://doi.org/10.1002/cssc.202200027).
- 9 M. Yu, E. Budiyo and H. Tüysüz, Principles of Water Electrolysis and Recent Progress in Cobalt-, Nickel-, and Iron-Based Oxides for the Oxygen Evolution Reaction, *Angew. Chem., Int. Ed.*, 2022, **61**(1), e202103824, DOI: [10.1002/anie.202103824](https://doi.org/10.1002/anie.202103824).
- 10 F. Dionigi and P. Strasser, NiFe-Based (Oxy)hydroxide Catalysts for Oxygen Evolution Reaction in Non-Acidic Electrolytes, *Adv. Energy Mater.*, 2016, **6**(23), 1600621, DOI: [10.1002/aenm.201600621](https://doi.org/10.1002/aenm.201600621).
- 11 S. Anantharaj, S. Kundu and S. Noda, “The Fe Effect”: A review unveiling the critical roles of Fe in enhancing OER activity of Ni and Co based catalysts, *Nano Energy*, 2021, **80**, 105514, DOI: [10.1016/j.nanoen.2020.105514](https://doi.org/10.1016/j.nanoen.2020.105514).
- 12 G. Młynarek, M. Paszkiewicz and A. Radniecka, The effect of ferric ions on the behaviour of a nickelous hydroxide electrode, *J. Appl. Electrochem.*, 1984, **14**(2), 145–149, DOI: [10.1007/BF00618733](https://doi.org/10.1007/BF00618733).
- 13 D. A. Corrigan, R. S. Conell, C. A. Fierro and D. A. Scherson, In-situ Mössbauer study of redox processes in a composite hydroxide of iron and nickel, *J. Phys. Chem.*, 1987, **91**(19), 5009–5011, DOI: [10.1021/j100303a024](https://doi.org/10.1021/j100303a024).
- 14 L. Trotochaud, S. L. Young, J. K. Ranney and S. W. Boettcher, Nickel–Iron Oxyhydroxide Oxygen-Evolution Electrocatalysts: The Role of Intentional and Incidental Iron Incorporation, *J. Am. Chem. Soc.*, 2014, **136**(18), 6744–6753, DOI: [10.1021/ja502379c](https://doi.org/10.1021/ja502379c).
- 15 M. S. Burke, M. G. Kast, L. Trotochaud, A. M. Smith and S. W. Boettcher, Cobalt–Iron (Oxy)hydroxide Oxygen Evolution Electrocatalysts: The Role of Structure and Composition on Activity, Stability, and Mechanism, *J. Am. Chem. Soc.*, 2015, **137**(10), 3638–3648, DOI: [10.1021/jacs.5b00281](https://doi.org/10.1021/jacs.5b00281).
- 16 L. J. Enman, M. B. Stevens, M. H. Dahan, M. R. Nellist, M. C. Toroker and S. W. Boettcher, Operando X-Ray Absorption Spectroscopy Shows Iron Oxidation Is Concurrent with Oxygen Evolution in Cobalt–Iron (Oxy)hydroxide Electrocatalysts, *Angew. Chem., Int. Ed.*, 2018, **57**(39), 12840–12844, DOI: [10.1002/anie.201808818](https://doi.org/10.1002/anie.201808818).
- 17 M. S. Burke, S. Zou, L. J. Enman, J. E. Kellon, C. A. Gabor and E. Pledger, *et al.*, Revised Oxygen Evolution Reaction Activity Trends for First-Row Transition-Metal (Oxy)hydroxides in Alkaline Media, *J. Phys. Chem. Lett.*, 2015, **6**(18), 3737–3742, DOI: [10.1021/acs.jpclett.5b01650](https://doi.org/10.1021/acs.jpclett.5b01650).
- 18 A. M. Smith, L. Trotochaud, M. S. Burke and S. W. Boettcher, Contributions to activity enhancement via Fe incorporation in Ni-(oxy)hydroxide/borate catalysts for near-neutral pH oxygen evolution, *Chem. Commun.*, 2015, **51**(25), 5261–5263, DOI: [10.1039/C4CC08670H](https://doi.org/10.1039/C4CC08670H).
- 19 M. B. Stevens, C. D. M. Trang, L. J. Enman, J. Deng and S. W. Boettcher, Reactive Fe-Sites in Ni/Fe (Oxy)hydroxide Are Responsible for Exceptional Oxygen Electrocatalysis Activity, *J. Am. Chem. Soc.*, 2017, **139**(33), 11361–11364, DOI: [10.1021/jacs.7b07117](https://doi.org/10.1021/jacs.7b07117).
- 20 X. Zheng, B. Zhang, P. De Luna, Y. Liang, R. Comin and O. Voznyy, *et al.*, Theory-driven design of high-valence metal sites for water oxidation confirmed using in situ soft X-ray absorption, *Nat. Chem.*, 2018, **10**(2), 149–154, DOI: [10.1038/nchem.2886](https://doi.org/10.1038/nchem.2886).
- 21 H. Xiao, H. Shin and W. A. Goddard, Synergy between Fe and Ni in the optimal performance of (Ni,Fe)OOH catalysts for the oxygen evolution reaction, *Proc. Natl. Acad. Sci. U. S. A.*, 2018, **115**(23), 5872–5877, DOI: [10.1073/pnas.1722034115](https://doi.org/10.1073/pnas.1722034115).
- 22 D. Y. Chung, P. P. Lopes, P. Farinazzo Bergamo Dias Martins, H. He, T. Kawaguchi and P. Zapol, *et al.*, Dynamic stability of active sites in hydr(oxy)oxides for the oxygen evolution reaction, *Nat. Energy*, 2020, **5**(3), 222–230, DOI: [10.1038/s41560-020-0576-y](https://doi.org/10.1038/s41560-020-0576-y).
- 23 X. Xie, L. Du, L. Yan, S. Park, Y. Qiu and J. Sokolowski, *et al.*, Oxygen Evolution Reaction in Alkaline Environment: Material Challenges and Solutions, *Adv. Funct. Mater.*, 2022, **32**(21), 2110036, DOI: [10.1002/adfm.202110036](https://doi.org/10.1002/adfm.202110036).
- 24 Z. Wang, W. A. Goddard and H. Xiao, Potential-dependent transition of reaction mechanisms for oxygen evolution on layered double hydroxides, *Nat. Commun.*, 2023, **14**(1), 4228, DOI: [10.1038/s41467-023-40011-8](https://doi.org/10.1038/s41467-023-40011-8).
- 25 T. Wu and Z. J. Xu, Oxygen evolution in spin-sensitive pathways, *Curr. Opin. Electrochem.*, 2021, **30**, 100804, DOI: [10.1016/j.coelec.2021.100804](https://doi.org/10.1016/j.coelec.2021.100804).
- 26 C. Lin, J. L. Li, X. Li, S. Yang, W. Luo and Y. Zhang, *et al.*, In-situ reconstructed Ru atom array on α -MnO₂ with enhanced performance for acidic water oxidation, *Nat. Catal.*, 2021, **4**(12), 1012–1023, DOI: [10.1038/s41929-021-00703-0](https://doi.org/10.1038/s41929-021-00703-0).
- 27 F. Dionigi, Z. Zeng, I. Sinev, T. Merzdorf, S. Deshpande and M. B. Lopez, *et al.*, In-situ structure and catalytic mechanism of NiFe and CoFe layered double hydroxides during oxygen evolution, *Nat. Commun.*, 2020, **11**(1), 2522, DOI: [10.1038/s41467-020-16237-1](https://doi.org/10.1038/s41467-020-16237-1).
- 28 J. Ferreira de Araújo, F. Dionigi, T. Merzdorf, H. S. Oh and P. Strasser, Evidence of Mars–Van Krevelen Mechanism in the Electrochemical Oxygen Evolution on Ni-Based Catalysts, *Angew. Chem., Int. Ed.*, 2021, **60**(27), 14981–14988, DOI: [10.1002/anie.202101698](https://doi.org/10.1002/anie.202101698).
- 29 D. Friebe, M. W. Louie, M. Bajdich, K. E. Sanwald, Y. Cai and A. M. Wise, *et al.*, Identification of Highly Active Fe Sites in (Ni,Fe)OOH for Electrocatalytic Water Splitting, *J. Am.*



- Chem. Soc.*, 2015, **137**(3), 1305–1313, DOI: [10.1021/ja511559d](#).
- 30 S. Klaus, Y. Cai, M. W. Louie, L. Trotochaud and A. T. Bell, Effects of Fe Electrolyte Impurities on Ni(OH)₂/NiOOH Structure and Oxygen Evolution Activity, *J. Phys. Chem. C*, 2015, **119**(13), 7243–7254, DOI: [10.1021/acs.jpcc.5b00105](#).
 - 31 M. K. Bates, Q. Jia, H. Doan, W. Liang and S. Mukerjee, Charge-Transfer Effects in Ni–Fe and Ni–Fe–Co Mixed-Metal Oxides for the Alkaline Oxygen Evolution Reaction, *ACS Catal.*, 2016, **6**(1), 155–161, DOI: [10.1021/acscatal.5b01481](#).
 - 32 M. Görlin, P. Chernev, J. Ferreira de Araújo, T. Reier, S. Dresp and B. Paul, *et al.*, Oxygen Evolution Reaction Dynamics, faradaic Charge Efficiency, and the Active Metal Redox States of Ni–Fe Oxide Water Splitting Electrocatalysts, *J. Am. Chem. Soc.*, 2016, **138**(17), 5603–5614, DOI: [10.1021/jacs.6b00332](#).
 - 33 M. Görlin, J. Ferreira de Araújo, H. Schmies, D. Bernsmeier, S. Dresp and M. Gliech, *et al.*, Tracking Catalyst Redox States and Reaction Dynamics in Ni–Fe Oxyhydroxide Oxygen Evolution Reaction Electrocatalysts: The Role of Catalyst Support and Electrolyte pH, *J. Am. Chem. Soc.*, 2017, **139**(5), 2070–2082, DOI: [10.1021/jacs.6b12250](#).
 - 34 N. Li, D. K. Bediako, R. G. Hadt, D. Hayes, T. J. Kempa and F. von Cube, *et al.*, Influence of iron doping on tetravalent nickel content in catalytic oxygen evolving films, *Proc. Natl. Acad. Sci. U. S. A.*, 2017, **114**(7), 1486–1491, DOI: [10.1073/pnas.1620787114](#).
 - 35 J. Halldin Stenlid, M. Görlin, O. Diaz-Morales, B. Davies, V. Grigorev and D. Degerman, *et al.*, Operando Characterization of Fe in Doped Ni_x(Fe_{1-x})O_yHz Catalysts for Electrochemical Oxygen Evolution, *J. Am. Chem. Soc.*, 2025, **147**(5), 4120–4134, DOI: [10.1021/jacs.4c13417](#).
 - 36 M. Balasubramanian, C. A. Melendres and S. Mini, X-ray Absorption Spectroscopy Studies of the Local Atomic and Electronic Structure of Iron Incorporated into Electrodeposited Hydrous Nickel Oxide Films, *J. Phys. Chem. B*, 2000, **104**(18), 4300–4306, DOI: [10.1021/jp9921710](#).
 - 37 J. Y. C. Chen, L. Dang, H. Liang, W. Bi, J. B. Gerken and S. Jin, *et al.*, Operando Analysis of NiFe and Fe Oxyhydroxide Electrocatalysts for Water Oxidation: Detection of Fe⁴⁺ by Mössbauer Spectroscopy, *J. Am. Chem. Soc.*, 2015, **137**(48), 15090–15093, DOI: [10.1021/jacs.5b10699](#).
 - 38 Z. Kuang, S. Liu, X. Li, M. Wang, X. Ren and J. Ding, *et al.*, Topotactically constructed nickel–iron (oxy)hydroxide with abundant *in-situ* produced high-valent iron species for efficient water oxidation, *J. Energy Chem.*, 2021, **57**, 212–218, DOI: [10.1016/j.jechem.2020.09.014](#).
 - 39 Z. K. Goldsmith, A. K. Harshan, J. B. Gerken, M. Vörös, G. Galli and S. S. Stahl, *et al.*, Characterization of NiFe oxyhydroxide electrocatalysts by integrated electronic structure calculations and spectroelectrochemistry, *Proc. Natl. Acad. Sci. U. S. A.*, 2017, **114**(12), 3050–3055, DOI: [10.1073/pnas.1702081114](#).
 - 40 D. Wang, J. Zhou, Y. Hu, J. Yang, N. Han and Y. Li, *et al.*, In Situ X-ray Absorption Near-Edge Structure Study of Advanced NiFe(OH)_x Electrocatalyst on Carbon Paper for Water Oxidation, *J. Phys. Chem. C*, 2015, **119**(34), 19573–19583, DOI: [10.1021/acs.jpcc.5b02685](#).
 - 41 L. Osmieri, H. Yu, R. P. Hermann, M. E. Kreider, H. M. Meyer and A. J. Kropf, *et al.*, Aerogel-derived nickel-iron oxide catalysts for oxygen evolution reaction in alkaline media, *Appl. Catal., B*, 2024, **348**, 123843, DOI: [10.1016/j.apcatb.2024.123843](#).
 - 42 M. E. Kreider, H. Yu, L. Osmieri, M. R. Parimuha, K. S. Reeves and D. H. Marin, *et al.*, Understanding the Effects of Anode Catalyst Conductivity and Loading on Catalyst Layer Utilization and Performance for Anion Exchange Membrane Water Electrolysis, *ACS Catal.*, 2024, **14**(14), 10806–10819, DOI: [10.1021/acscatal.4c02932](#).
 - 43 J. Park and D. J. Myers, Novel platinum group metal-free catalyst ink deposition system for combinatorial polymer electrolyte fuel cell performance evaluation, *J. Power Sources*, 2020, **480**, 228801, DOI: [10.1016/j.jpowsour.2020.228801](#).
 - 44 C. U. Segre, N. E. Leyarowska, L. D. Chapman, W. M. Lavender, P. W. Plag and A. S. King, *et al.*, The MRCAT insertion device beamline at the Advanced Photon Source, *AIP Conf. Proc.*, 2000, **521**(1), 419–422, DOI: [10.1063/1.1291825](#).
 - 45 B. Ravel and M. Newville, ATHENA, ARTEMIS, HEPHAESTUS: data analysis for X-ray absorption spectroscopy using IFEFFIT, *J. Synchrotron Radiat.*, 2005, **12**(4), 537–541, DOI: [10.1107/S0909049505012719](#).
 - 46 O. Diaz-Morales, D. Ferrus-Suspedra and M. T. M. Koper, The importance of nickel oxyhydroxide deprotonation on its activity towards electrochemical water oxidation, *Chem. Sci.*, 2016, **7**(4), 2639–2645, DOI: [10.1039/C5SC04486C](#).
 - 47 J. Suntivich, H. A. Gasteiger, N. Yabuuchi and Y. Shao-Horn, Electrocatalytic Measurement Methodology of Oxide Catalysts Using a Thin-Film Rotating Disk Electrode, *J. Electrochem. Soc.*, 2010, **157**(8), B1263, DOI: [10.1149/1.3456630](#).
 - 48 A. Wattiaux, L. Fournès, A. Demourgues, N. Bernabén, J. C. Grenier and M. Pouchard, A novel preparation method of the SrFeO₃ cubic perovskite by electrochemical means, *Solid State Commun.*, 1991, **77**(7), 489–493, DOI: [10.1016/0038-1098\(91\)90726-C](#).
 - 49 L. Guerlou-Demourgues, L. Fournès and C. Delmas, In Situ ⁵⁷Fe Mössbauer Spectroscopy Study of the Electrochemical Behavior of an Iron-Substituted Nickel Hydroxide Electrode, *J. Electrochem. Soc.*, 1996, **143**(10), 3083, DOI: [10.1149/1.1837168](#).
 - 50 A. A. Kamnev, B. B. Ezhov, V. Rusanov and V. Angelov, Application of transmission Mössbauer effect spectroscopy to the study of electrocatalysis and adsorption phenomena at the nickel hydroxide electrode, *Surf. Interface Anal.*, 1992, **19**(1–12), 577–580, DOI: [10.1002/sia.7401901107](#).
 - 51 O. Haas, C. H. R. Ludwig, U. Bergmann, R. N. Singh, A. Braun and T. Graule, X-ray absorption investigation of the valence state and electronic structure of La_{1-x}Ca_xCoO_{3-δ} in comparison with La_{1-x}Sr_xCoO_{3-δ} and La_{1-x}Sr_xFeO_{3-δ}, *J. Solid State Chem.*, 2011, **184**(12), 3163–3171, DOI: [10.1016/j.jssc.2011.09.027](#).



- 52 J. Blasco, B. Aznar, J. García, G. Subías, J. Herrero-Martín and J. Stankiewicz, Charge disproportionation in $\text{La}_{1-x}\text{Sr}_x\text{FeO}_3$ probed by diffraction and spectroscopic experiments, *Phys. Rev. B: Condens. Matter Mater. Phys.*, 2008, **77**(5), 054107, DOI: [10.1103/PhysRevB.77.054107](https://doi.org/10.1103/PhysRevB.77.054107).
- 53 O. Glemser and J. Einerhand, Die Struktur höherer Nickelhydroxyde, *Z. Anorg. Chem.*, 1950, **261**(1–2), 43–51, DOI: [10.1002/zaac.19502610104](https://doi.org/10.1002/zaac.19502610104).
- 54 M. Casas-Cabanas, M. D. Radin, J. Kim, C. P. Grey, A. V. der Ven and M. R. Palacín, The nickel battery positive electrode revisited: stability and structure of the β -NiOOH phase, *J. Mater. Chem. A*, 2018, **6**(39), 19256–19265, DOI: [10.1039/C8TA07460G](https://doi.org/10.1039/C8TA07460G).
- 55 P. C. M. Laan, F. J. de Zwart, E. M. Wilson, A. Troglia, O. C. M. Lugier and N. J. Geels, *et al.*, Understanding the Oxidative Properties of Nickel Oxyhydroxide in Alcohol Oxidation Reactions, *ACS Catal.*, 2023, **13**(13), 8467–8476, DOI: [10.1021/acscatal.3c01120](https://doi.org/10.1021/acscatal.3c01120).
- 56 X. Z. Fu, Y. J. Zhu, Q. C. Xu, J. Li, J. H. Pan and J. Q. Xu, *et al.*, Nickel oxyhydroxides with various oxidation states prepared by chemical oxidation of spherical β -Ni(OH)₂, *Solid State Ionics*, 2007, **178**(13), 987–993, DOI: [10.1016/j.ssi.2007.04.011](https://doi.org/10.1016/j.ssi.2007.04.011).
- 57 D. A. Corrigan and R. M. Bendert, Effect of Coprecipitated Metal Ions on the Electrochemistry of Nickel Hydroxide Thin Films: Cyclic Voltammetry in 1M KOH, *J. Electrochem. Soc.*, 1989, **136**(3), 723, DOI: [10.1149/1.2096717](https://doi.org/10.1149/1.2096717).
- 58 L. Liu, Z. Zhou and C. Peng, Sonochemical intercalation synthesis of nano γ -nickel oxyhydroxide: Structure and electrochemical properties, *Electrochim. Acta*, 2008, **54**(2), 434–441, DOI: [10.1016/j.electacta.2008.07.055](https://doi.org/10.1016/j.electacta.2008.07.055).
- 59 D. S. Hall, D. J. Lockwood, C. Bock and B. R. MacDougall, Nickel hydroxides and related materials: a review of their structures, synthesis and properties, *Proc. R. Soc., Ser. A*, 2015, **471**(2174), 20140792, DOI: [10.1098/rspa.2014.0792](https://doi.org/10.1098/rspa.2014.0792).
- 60 K. I. Pandya, W. E. O'Grady, D. A. Corrigan, J. McBreen and R. W. Hoffman, Extended X-ray absorption fine structure investigations of nickel hydroxides, *J. Phys. Chem.*, 1990, **94**(1), 21–26, DOI: [10.1021/j100364a005](https://doi.org/10.1021/j100364a005).
- 61 T. Malis, S. C. Cheng and R. F. Egerton, EELS log-ratio technique for specimen-thickness measurement in the TEM, *J. Electron Microsc. Tech.*, 1988, **8**(2), 193–200, DOI: [10.1002/jemt.1060080206](https://doi.org/10.1002/jemt.1060080206).
- 62 R. S. McEwen, Crystallographic studies on nickel hydroxide and the higher nickel oxides, *J. Phys. Chem.*, 1971, **75**(12), 1782–1789, DOI: [10.1021/j100681a004](https://doi.org/10.1021/j100681a004).
- 63 M. Taibi, S. Ammar, F. Schoenstein, N. Jouini, F. Fiévet and T. Chauveau, *et al.*, Powder and film of nickel and iron-layered double hydroxide: Elaboration in polyol medium and characterization, *J. Phys. Chem. Solids*, 2008, **69**(5), 1052–1055, DOI: [10.1016/j.jpcs.2007.10.115](https://doi.org/10.1016/j.jpcs.2007.10.115).
- 64 P. Acharya, J. Hong, R. Manso, A. S. Hoffman, L. Kekedy-Nagy and J. Chen, *et al.*, Temporal Ni K-Edge X-ray Absorption Spectroscopy Study Reveals the Kinetics of the Ni Redox Behavior of the Iron-Nickel Oxide Bimetallic OER Catalyst, *J. Phys. Chem. C*, 2023, **127**(25), 11891–11901, DOI: [10.1021/acs.jpcc.3c03480](https://doi.org/10.1021/acs.jpcc.3c03480).
- 65 R. Goel, R. Jha and C. Ravikant, Investigating the structural, electrochemical, and optical properties of p-type spherical nickel oxide (NiO) nanoparticles, *J. Phys. Chem. Solids*, 2020, **144**, 109488, DOI: [10.1016/j.jpcs.2020.109488](https://doi.org/10.1016/j.jpcs.2020.109488).
- 66 D. M. MacArthur, The Proton Diffusion Coefficient for the Nickel Hydroxide Electrode, *J. Electrochem. Soc.*, 1970, **117**(6), 729, DOI: [10.1149/1.2407618](https://doi.org/10.1149/1.2407618).
- 67 K. P. Ta and J. Newman, Mass Transfer and Kinetic Phenomena at the Nickel Hydroxide Electrode, *J. Electrochem. Soc.*, 1998, **145**(11), 3860, DOI: [10.1149/1.1838886](https://doi.org/10.1149/1.1838886).
- 68 H. S. Kim, T. Itoh, M. Nishizawa, M. Mohamedi, M. Umeda and I. Uchida, Microvoltammetric study of electrochemical properties of a single spherical nickel hydroxide particle, *Int. J. Hydrogen Energy*, 2002, **27**(3), 295–300, DOI: [10.1016/S0360-3199\(01\)00118-5](https://doi.org/10.1016/S0360-3199(01)00118-5).
- 69 G. W. D. Briggs and P. R. Snodin, Ageing and the diffusion process at the nickel hydroxide electrode, *Electrochim. Acta*, 1982, **27**(5), 565–572, DOI: [10.1016/0013-4686\(82\)85041-X](https://doi.org/10.1016/0013-4686(82)85041-X).
- 70 L. Bing, Y. Huatang, Z. Yunshi, Z. Zuoxiang and S. Deying, Cyclic voltammetric studies of stabilized α -nickel hydroxide electrode, *J. Power Sources*, 1999, **79**(2), 277–280, DOI: [10.1016/S0378-7753\(99\)00053-1](https://doi.org/10.1016/S0378-7753(99)00053-1).
- 71 H. S. Ahn and A. J. Bard, Surface Interrogation Scanning Electrochemical Microscopy of Ni_{1-x}Fe_xOOH (0 < x < 0.27) Oxygen Evolving Catalyst: Kinetics of the “fast” Iron Sites, *J. Am. Chem. Soc.*, 2016, **138**(1), 313–318, DOI: [10.1021/jacs.5b10977](https://doi.org/10.1021/jacs.5b10977).
- 72 Y. Ou, L. P. Twight, B. Samanta, L. Liu, S. Biswas and J. L. Fehrs, *et al.*, Cooperative Fe sites on transition metal (oxy)hydroxides drive high oxygen evolution activity in base, *Nat. Commun.*, 2023, **14**(1), 7688, DOI: [10.1038/s41467-023-43305-z](https://doi.org/10.1038/s41467-023-43305-z).

